SANDIA REPORT

SAND2021-11377 Printed September 2021



Application of Refractory High-Entropy Alloys for Higher-Reliability and Higher-Efficiency Brayton Cycles and Advanced Nuclear Reactors

Sal Rodriguez, Eric Lang, Nick Argibay, Andrew Kustas, Erin Barrick, Morgan Jones, Ed Arata, Chuck Walker, Graham Monroe, Shaun Whetten, Dennis De Smet, and Hannah H. Lim

Prepared by Sandia National Laboratories Albuquerque, New Mexico 87185 and Livermore, California 94550 Issued by Sandia National Laboratories, operated for the United States Department of Energy by National Technology & Engineering Solutions of Sandia, LLC.

NOTICE: This report was prepared as an account of work sponsored by an agency of the United States Government. Neither the United States Government, nor any agency thereof, nor any of their employees, nor any of their contractors, subcontractors, or their employees, make any warranty, express or implied, or assume any legal liability or responsibility for the accuracy, completeness, or usefulness of any information, apparatus, product, or process disclosed, or represent that its use would not infringe privately owned rights. Reference herein to any specific commercial product, process, or service by trade name, trademark, manufacturer, or otherwise, does not necessarily constitute or imply its endorsement, recommendation, or favoring by the United States Government, any agency thereof, or any of their contractors or subcontractors. The views and opinions expressed herein do not necessarily state or reflect those of the United States Government, any agency thereof, or any of their contractors.

Printed in the United States of America. This report has been reproduced directly from the best available copy.

Available to DOE and DOE contractors from

U.S. Department of Energy Office of Scientific and Technical Information P.O. Box 62 Oak Ridge, TN 37831

Telephone: (865) 576-8401 Facsimile: (865) 576-5728 E-Mail: reports@osti.gov

Online ordering: http://www.osti.gov/scitech

Available to the public from

U.S. Department of Commerce National Technical Information Service 5301 Shawnee Rd Alexandria, VA 22312

Telephone: (800) 553-6847 Facsimile: (703) 605-6900 E-Mail: orders@ntis.gov

Online order: https://classic.ntis.gov/help/order-methods/



ABSTRACT

An exceptional set of newly-discovered advanced superalloys known as refractory high-entropy alloys (RHEAs) can provide near-term solutions for wear, erosion, corrosion, high-temperature strength, creep, and radiation issues associated with supercritical carbon dioxide (sCO2) Brayton Cycles and advanced nuclear reactors. In particular, these superalloys can significantly extend their durability, reliability, and thermal efficiency, thereby making them more cost-competitive, safer, and reliable.

For this project, it was endeavored to manufacture and test certain RHEAs, to solve technical issues impacting the Brayton Cycle and advanced nuclear reactors. This was achieved by leveraging Sandia's patents, technical advances, and previous experience working with RHEAs.

Herein, three RHEA manufacturing methods were applied: laser engineered net shaping, spark plasma sintering, and spray coating. Two promising RHEAs were selected, HfNbTaZr and MoNbTaVW. To demonstrate their performance, erosion, structural, radiation, and high-temperature experiments were conducted on the RHEAs, stainless steel (SS) 316 L, SS 1020, and Inconel 718 test coupons, as well as bench-top components. The experimental data is presented, analyzed, and confirms the superior performance of the HfNbTaZr and MoNbTaVW RHEAs vs. SS 316 L, SS 1020, and Inconel 718. In addition, to gain more insights for larger-scale RHEA applications, the erosion and structural capabilities for the two RHEAs were simulated and compared with the experimental data.

The experimental data confirm the superior performance of the HfNbTaZr and MoNbTaVW RHEAs vs. SS and Inconel. Most importantly, the erosion and the coating material experimental data show that erosion in sCO2 Brayton Cycles can be eliminated completely if RHEAs are used. The experimental suite and validations confirm that HfNbTaZr is suitable for harsh environments that do not include nuclear radiation, while MoNbTaVW is suitable for harsh environments that include radiation.

This page left blank

CONTENTS

1.	Introduction	11
	1.1. Introduction to RHEAs	11
	1.2. Previous RHEA Work Conducted at Sandia National Laboratories as of 2021	14
2.	RHEA Composition Selection	16
	2.1. The HfNbTaZr RHEA	
	2.2. The MoNbTaVW RHEA	20
3.	RHEA Experiments and Data	22
٠.	3.1. Manufactured RHEA Test Coupons and Components	
	3.2. RHEA Radiation Testing at the Ion Beam Lab	
	3.3. RHEA Erosion Testing	
	3.4. RHEA IBL Structural and Thermal Testing	
	3.5. RHEA Tube Manufacturing and Pressurization Test	
	3.6. RHEA Coating Experimental Data	
4.	RHEA Simulations	38
	4.1. RHEA Tube Pressurization Test Simulations	
	4.2. RHEA Erosion Simulations	40
5.	RHEA Applications	43
٠.	5.1. Advanced Nuclear Reactors	
	5.2. Energy Conversion Cycles	
6.	SUMMARY AND Conclusion	
Fig	gure 0-1. Erosion experimental data and modeling of an sCO2 loop diffuser component. The region circled with the red dashed loop shows where erosion is	
	prevalent	
	gure 1-1. Five extraordinary RHEA material properties	
	gure 1-2. The 16 refractory elements.	
	gure 1-3. The random atomic distribution of a well-mixed RHEAgure 1-4. RLEA and RHEA test samples printed at SNL during 2020 using the LENS	14
1.15	approach	15
Fig	gure 1-5. NbTaVW RHEA Type A dogbone specimens printed via the LENS machine	
	gure 2-1. SEM image for HfNbTaZr with a ruler scale set to 50 microns	۱٦
_		
		18
	gure 2-2. SEM image for HfNbTaZr with a ruler scale set to 5 micronsgure 2-3. EDS image for HfNbTaZr	18 18
Fig	gure 2-2. SEM image for HfNbTaZr with a ruler scale set to 5 microns	18 18 19
	gure 2-2. SEM image for HfNbTaZr with a ruler scale set to 5 micronsgure 2-3. EDS image for HfNbTaZrgure 2-4. Polished HfNbTaZr RHEA samplegure 2-5. EBSD image for HfNbTaZr with a ruler scale set to 2 microns (RHS) and 5 microns	18 18 19
Fig	gure 2-2. SEM image for HfNbTaZr with a ruler scale set to 5 micronsgure 2-3. EDS image for HfNbTaZrgure 2-4. Polished HfNbTaZr RHEA samplegure 2-5. EBSD image for HfNbTaZr with a ruler scale set to 2 microns (RHS) and 5 microns (LHS)	18 19 19
Fig Fig	gure 2-2. SEM image for HfNbTaZr with a ruler scale set to 5 microns. gure 2-3. EDS image for HfNbTaZr. gure 2-4. Polished HfNbTaZr RHEA sample gure 2-5. EBSD image for HfNbTaZr with a ruler scale set to 2 microns (RHS) and 5 microns (LHS)	18 19 19 20
Fig Fig	gure 2-2. SEM image for HfNbTaZr with a ruler scale set to 5 microns	18 19 19 20 23
Fig Fig Fig	gure 2-2. SEM image for HfNbTaZr with a ruler scale set to 5 microns. gure 2-3. EDS image for HfNbTaZr. gure 2-4. Polished HfNbTaZr RHEA sample gure 2-5. EBSD image for HfNbTaZr with a ruler scale set to 2 microns (RHS) and 5 microns (LHS)	18 19 19 20 23
Fig Fig Fig Fig	gure 2-2. SEM image for HfNbTaZr with a ruler scale set to 5 microns. gure 2-3. EDS image for HfNbTaZr. gure 2-4. Polished HfNbTaZr RHEA sample gure 2-5. EBSD image for HfNbTaZr with a ruler scale set to 2 microns (RHS) and 5 microns (LHS)	18 19 19 20 23
Fig Fig Fig Fig	gure 2-2. SEM image for HfNbTaZr with a ruler scale set to 5 microns. gure 2-3. EDS image for HfNbTaZr. gure 2-4. Polished HfNbTaZr RHEA sample	18 19 19 20 23 24

Figure 3-6. SEM image of LENS MoNbTaVW at 100 micron scale	25
Figure 3-7. HVOF RHEA coatings. 1=Inconel 718 HfNbTaZr and 2=SS 321 HfNbTaZr;	
3=Inconel 718 MoNbTaVW and 4=SS 321 MoNbTaVW	26
Figure 3-8. APS RHEA coatings. A=Inconel 718 MoNbTaVW and B=SS 321 MoNbTaVW;	
C=Inconel 718 HfNbTaZr and D=SS 321 HfNbTaZr	26
Figure 3-9. Annealed HfNbTaZr and MoNbTaVW test pieces.	28
Figure 3-10. IBL capabilities.	
Figure 3-11. Erosion test set-up.	30
Figure 3-12. Cumulative eroded mass vs. time for the SS 1020, SS 314, Inconel 718, untreated	
base case HfNbTaZr, and three post-processed HfNbTaZr plates	31
Figure 3-13. One inch HfNbTaZr RHEA tube segment.	
Figure 3-14. Annealed 1 inch HfNbTaZr RHEA tube.	33
Figure 3-15. RHEA coating ramped scratch test.	34
Figure 3-16. Applied normal force distribution in the four RHEA coatings	35
Figure 3-17. Coefficient of friction for the four RHEA coatings.	
Figure 3-18. Hardness vs. strain rate for the four RHEA coatings.	36
Figure 4-1. Adagio structural mechanics model for the RHEA tube.	38
Figure 4-2. Comparison of displacement at yielding for Inconel 718 (left) and HfNbTaZr (right	nt)40
Figure 4-3. Comparison of von Mises stress state at yielding for Inconel 718 (left) and HfNbT	aZr
(right)	40
Figure 4-4. Erosion benchmark simulations for code validation.	
Figure 4-5. Erosion simulation model.	42
LIST OF TABLES	
Table 2-1. Some characteristics of the HfNbTaZr RHEA.	
Table 2-2. Some characteristics of the MoNbTaVW RHEA.	
Table 4-1. Elastic material properties of Inconel 718.	
Table 4-2. Elastic material properties of HfNbTaZr.	39
Table 4-3. CFD/FSI erosion simulation output	42

EXECUTIVE SUMMARY

Significant levels of erosion can occur in supercritical carbon dioxide (sCO2) Brayton Cycle components. The figure below shows an example of an eroded diffuser in a Brayton Cycle [Fleming et al., 2014], as well as recent advances in coupled computational fluid dynamics and structural modeling.

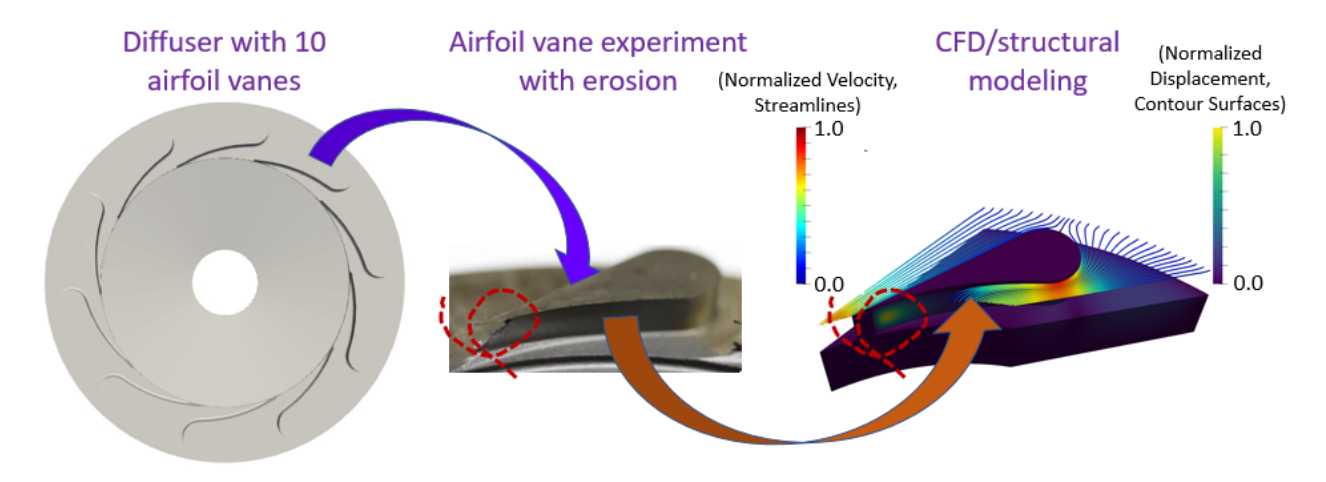


Figure 0-1. Erosion experimental data and modeling of an sCO2 loop diffuser component. The region circled with the red dashed loop shows where erosion is prevalent.

Therefore, refractory high-entropy alloy (RHEA) combinations suitable for more durable, reliable, and efficient energy cycles and advanced nuclear reactors were selected, manufactured, tested experimentally, and validated using Multiphysics modeling. The work presented herein shows that certain RHEAs can provide exceptional near-term solutions associated with sCO2 Brayton Cycles and advanced nuclear reactors. These include reduced wear, erosion, and radiation damage. Moreover, RHEAs have high-temperature strength, which is critical for achieving higher thermal efficiency.

To reduce technical risk and to expedite the material solutions associated with the selection, manufacturing, and testing of the RHEAs,

- Recent Sandia National Laboratories technical advances and patents were leveraged,
- Two promising RHEAs (HfNbTaZr and MoNbTaVW) were selected for their ability to thrive under harsh environments,
- Three independent RHEA manufacturing methods were applied,
- A suite of erosion, structural, radiation, and high-temperature experiments were conducted on the manufactured RHEAs,
- The RHEA performance was compared with typical materials used in energy conversion cycles, nuclear reactors, and similar industrial applications, such as SS 316 L, SS 1020, and Inconel 718, and
- Erosion Multiphysics and structural dynamics simulations were compared with the experimental data.

The experimental data confirms the superior performance of the HfNbTaZr and MoNbTaVW RHEAs vs stainless steel and Inconel, showing that HfNbTaZr is suitable for harsh, non-radiation environments, while MoNbTaVW is suitable for harsh environments that include radiation. Moreover, the erosion and the coating material properties experimental data show a strong potential for significant reduction of erosion in RHEA-coated sCO2 Brayton Cycle components, and this is further confirmed via structural and erosion modeling.

ACRONYMS AND DEFINITIONS

Abbreviation	Definition
AM	additive manufacturing
APS	air plasma spray
BCC	body-centered cubic
CFD	computational fluid dynamics
DPA	displacements per atom
EBSD	electron backscatter diffraction
EDS	energy dispersive x-ray spectroscopy
FSI	fluid-solid interaction
HEA	high-entropy alloy
HVOF	high velocity oxygen fuel
IBL	Ion Beam Lab
IPL	Integrated Program List
LB-DED	laser beam directed energy deposition
LENS	laser engineered net shape
LHS	left hand side
RMEO	refractory medium-entropy oxide
MS	molten salt
RCBC	recompression closed Brayton cycle
RHEA	refractory high-entropy alloy
RHS	right hand side
RLEA	refractory low-entropy alloy
RLEO	refractory low-entropy oxide
RT	room temperature
sCO2	supercritical carbon dioxide
SEM	scanning electron microscope
SNL	Sandia National Laboratories
SPS	spark plasma sintering
SS	stainless steel
STEP	supercritical transformational electric power

Abbreviation	Definition	
TEM	transmission electron microscope	
UNM	University of New Mexico	
VHTR	very high temperature reactor	
Z	number of protons (AKA atomic number)	

1. INTRODUCTION

The fascinating and near-term potential of high-entropy alloys (HEAs) and refractory high-entropy alloys (RHEAs) is presented in Section 1.1. The section also presents a brief primer for RHEAs. Section 1.2 describes RHEA progress at Sandia National Laboratories as of 2021. Note that beginning Section 2, this document solely describes RHEA progress based on the tasks performed as part of the Supercritical Transformational Electric Power (STEP) program associated with the Integrated Program List (IPL) for DOE-NE programs.

For this project, it was endeavored to exceed the current size of manufactured RHEA components, to achieve a range of several inches, and to have the test pieces undergo rigorous experimental testing. Consequently, two key RHEAs were selected, HfNbTaZr and MoNbTaVW. The selection rationale and methodology are presented in Section 2. Then, two RHEAs were built via three distinct advanced manufacturing approaches: laser engineered net shape (LENS) additive manufacturing (AM), spark plasma sintering (SPS), and spray coating. The RHEA test pieces were manufactured as small and mid-sized test coupons, as well as bench-top components. Thereafter, the manufactured pieces were subjected to various post manufacturing processes, including annealing and polishing. The test specimens were subjected to radiation, structural, and erosion tests, and their experimental performance data was compared with stainless steel (SS) 316 L, SS 1020, and Inconel 718. The experiments and experimental data are presented in Section 3. For validation purposes and to obtain insights for expediting large-scale RHEA components, coupled computational fluid dynamics (CFD) and structural models were developed to compare with erosion experimental data. In addition, a structural dynamics model was developed for a pressurized RHEA tube. The models are discussed in Section 4. Finally, Section 5 describes RHEA applications for near-term solutions for advanced nuclear reactors, energy conversion cycles, and aerospace components.

1.1. Introduction to RHEAs

HEAs in equiatomic combinations have been shown to have self-healing properties when exposed to radiation, and hence, have gained interest for advanced nuclear reactors [Liaw, 2014]. Refractory highentropy alloys (RHEAs) were first manufactured in 2010 as a solution for high-temperature aerospace applications; refractory elements have significant strength at elevated temperatures [Senkov et al., 2010; Miracle and Senkov, 2017; Senkov et al., 2018; Murty, Yeh, Ranganathan, and Bhattacharjee, 2019]. Since then, much progress has been made, and several useful RHEA properties have been observed experimentally and validated computationally [Senkov et al., 2010; Miracle and Senkov, 2017; Senkov et al., 2018; Murty, Yeh, Ranganathan, and Bhattacharjee, 2019; Rodriguez, Kustas, and Monroe, 2020]. In particular, certain RHEA combinations have up to five outstanding material properties that can provide near-term solutions for advanced nuclear reactors and high-efficiency, high-reliability power conversion cycles. As shown in Figure 1-1, these include:

- High yield stress at elevated temperature,
- Corrosion/erosion resistance,
- Radiation resistance,
- Self-healing, and

• Creep resistance.

Properties of Top-Notch RHEAs

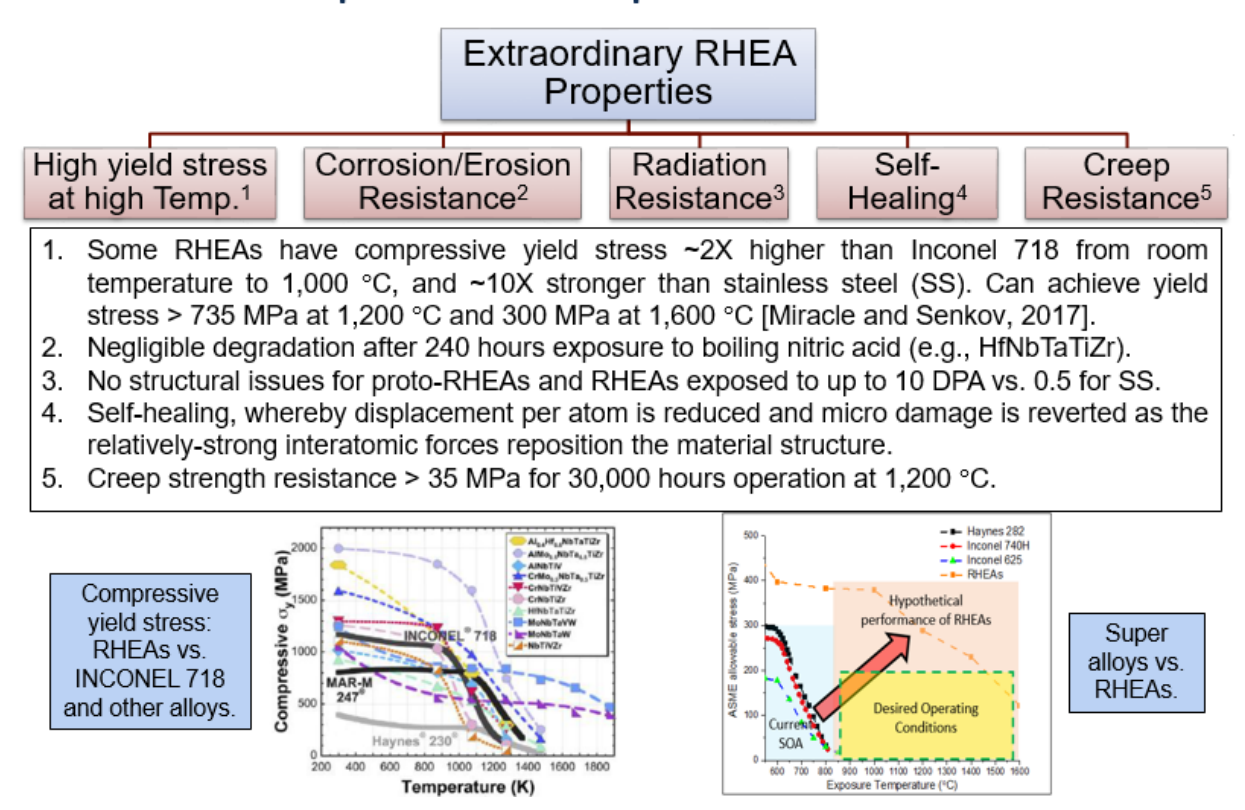


Figure 1-1. Five extraordinary RHEA material properties.

The above key properties translate into near-term solutions for nuclear reactors and power conversion cycles, such as

- Increased component durability (e.g., less wear, abrasion, erosion, corrosion, and creep),
- Radiation resistance,
- Higher operating temperature for higher thermal-efficiency performance (e.g., higher electrical output), and
- Higher structural strength in excess of 1,200 to 1,600 °C, making RHEAs suitable for advanced, very high temperature nuclear reactors.

Thus, certain RHEAs are ideal for components subject to harsh environments, such as high levels of wear, abrasion, creep, radiation, and oxidation. This includes seals, turbomachinery, nozzles, heat exchangers, and piping. For energy applications, a higher operating temperature translates to higher power efficiency if a high-efficiency energy conversion cycle is used, e.g. an sCO2 Recompression Closed Brayton Cycle (RCBC) [Rodriguez, 2017; Rodriguez et al., 2021]. Therefore, so long as the economics support it, it is desirable to operate in the 700 to 1,000 °C range in the near term, with long-term operation goals in the 1,000 to 1,500 °C range. Under such scenarios, RHEA coatings can

provide significant near- and long-term solutions for concentrated solar power, advanced hightemperature nuclear reactors (e.g., both gas and molten salt), high-efficiency power conversion units (e.g., sCO2 Recompression Closed Brayton Cycles), and high-temperature combustion cycles (e.g., Allam Cycles) [Feng et al., 2017; Kim et al., 2019; Rodriguez, Kustas, and Monroe, 2020; Rodriguez et al., 2021].

RHEAs typically consist of equiatomic combinations of four to six refractory elements from the 16 high-temperature refractory elements in the periodic table, as shown in Figure 1-2 [Senkov et al., 2010; Miracle and Senkov, 2017; Senkov et al., 2018; Murty, Yeh, Ranganathan, and Bhattacharjee, 2019]. Note that an equiatomic composition increases the solid solution entropy of the material, which is a measure of the ability of the material to mix. Therefore, the alloy can reach a higher degree of homogeneity, which can remarkably increase the material strength beyond the capacity of any one of its individual components. For example, the yield strength of HfNbTaZr is about 2,125 MPa. By contrast, the yield stress of individual components based solely on either Hf, Nb, Ta, or Zr, is approximately 125 to 362, 50.3 to 207, 380, and 230 MPa, respectively; clearly, the RHEA composition is much stronger than the individual components. For various reasons, including higher entropy generation, the aperiodic random distribution of the refractory elements increases the material performance metrics [Nagase et al., 2013; Liaw, 2014]. Figure 1-3 shows the random, aperiodic distribution of the atoms within a RHEA segment. For convenience, each atom type has a different color, so the aperiodicity can be observed.

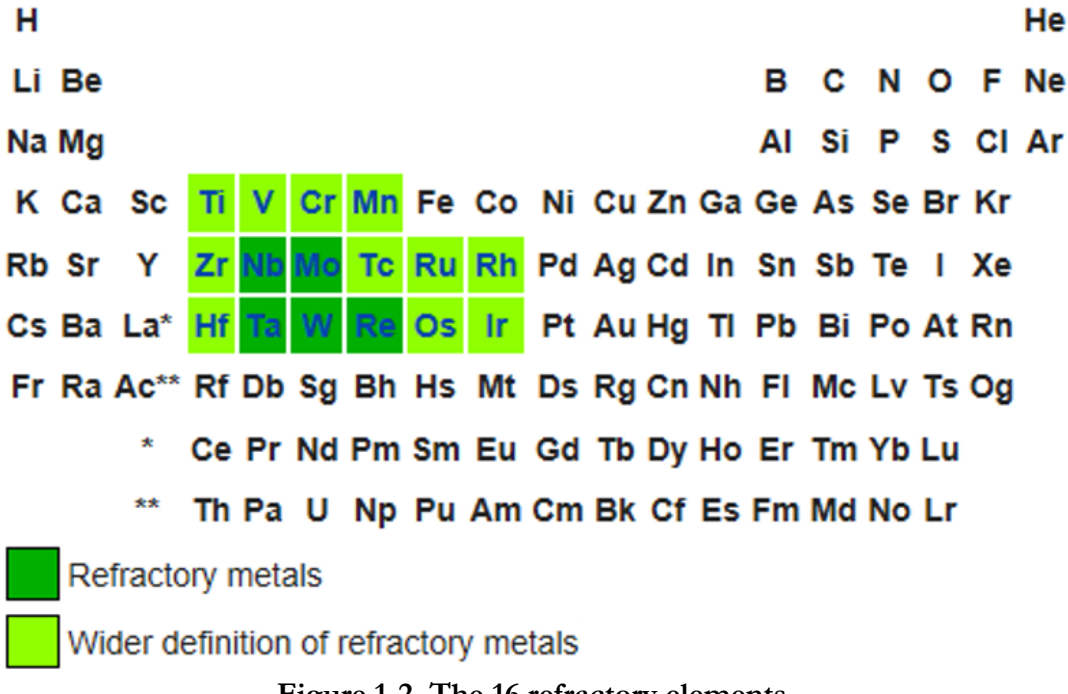


Figure 1-2. The 16 refractory elements.

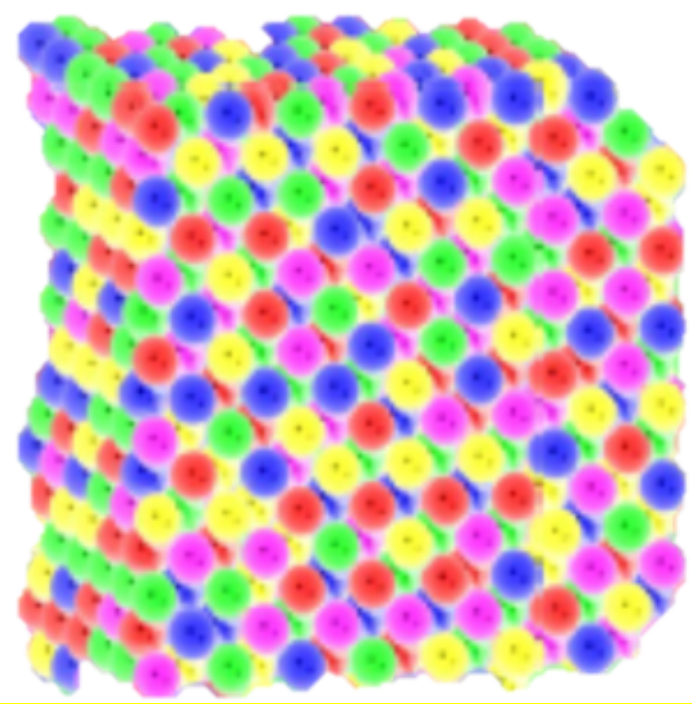


Figure 1-3. The random atomic distribution of a well-mixed RHEA.

1.2. Previous RHEA Work Conducted at Sandia National Laboratories as of 2021

Because of its promising properties and application space, small test samples for the refractory low-entropy alloy (RLEA) NbTa and the NbTaVW RHEA were printed at Sandia in 2019 using the laser engineered net shaping (LENS) approach. Figure 1-4 shows several RLEA and RHEA test samples that were printed at SNL via the LENS process in 2020, including MoNbTa, NbTaTi, MoNbTaW, and MoNbTaTi [Rodriguez, Kustas, and Monroe, 2020]. During the latter part of 2020, NbTaVW Type A dogbone specimens were printed using the LENS machine, as shown in Figure 1-5. The specimens confirmed Sandia's ability to print more complex RHEA shapes and allowed Sandia to perform detailed characterization tests. The manufacturing knowledge gained from these earlier efforts was leveraged onto the manufacturing of the two RHEAs of interest for this report, HfNbTaZr and MoNbTaVW.



Figure 1-4. RLEA and RHEA test samples printed at SNL during 2020 using the LENS approach.



Figure 1-5. NbTaVW RHEA Type A dogbone specimens printed via the LENS machine.

2. RHEA COMPOSITION SELECTION

A methodology was developed to down-select RHEAs based on economics and harsh-environment survivability, including erosion, corrosion, high temperature, and radiation [Rodriguez, Kustas, and Ames, 2020]. Reasonable down selections can be made to further reduce technical risk. For example, for nuclear reactors, the refractory alloys can be formed from well-known, reactor-compatible refractory elements, including Cr, Hf, Mo, Nb, Re, Ta, V, and Zr; recent combinations show strong resistance to radiation, corrosion, and creep-damage [Baranova, 2019; Wright, 2020]. For other energy and aerospace applications, a reasonable risk-mitigating strategy considers the existent refractory element composition of Inconel, and then modifies the composition such that equiatomic refractory-element superalloys are manufactured.

Refractory elements and alloys are noted for having excellent wear and abrasion resistance, e.g., HfNbTiZr, MoNbTaVW, and MoNbTaTiZr [Poulia et al., 2017; Senkov et al., 2018; Meghwal et al., 2020]. The following refractory elements, Mo, Nb, Re, Ta, and W, have varying degrees of creep resistance [Corrosionpedia, 2021]. Though prone to oxidation, some RHEAs tend to form complex protective oxide layers that can inhibit oxidation at elevated temperatures, similarly to aluminum. Such refractory elements include Cr, Mo, Ta, Ti, W, and Zr. However, simple oxides can also be formed, such as Cr₂O₃, MoO₃, Ta₂O, Ta₂O₅, TiO₂, WO₂, WO₃, and ZrO₂ [Jayaraj et al., 2017; Senkov et al., 2018; Mueller et al., 2019]. More complex oxides can take the form of refractory low-entropy oxides (RLEOs), such as CrTaO₄, which is found to reduce oxidation significantly as the rate kinetics is reduced from quartic to parabolic [Mueller et al., 2019]. Most interestingly, Ti in the presence of Cr and Ta acts as a catalyst, enabling the formation of the protective oxide layer, CrTaO₄ [Mueller et al., 2019]. In addition, RHEA oxidation can form refractory medium-entropy oxides (RMEOs), such as CrNbVO₆, CrNbTiVO₂, and Nb₂TiO₇ [Senkov et al., 2018].

Herein, two equiatomic-composition RHEAs based on HfNbTaZr and MoNbTaVW were considered for harsh environment applications. Equiatomic compositions were selected because this increases the solid solution entropy, and hence the innate ability of the RHEA to approach a higher degree of homogeneity, which ultimately increases material strength. It is shown in Section 2.1 that HfNbTaZr is suitable for harsh environment applications that do not include nuclear radiation, while Section 2.2 shows that MoNbTaVW is suitable for harsh environment applications that include radiation.

2.1. The HfNbTaZr RHEA

Key HfNbTaZr RHEA properties are summarized in Table 2-1. For convenience, the table is color-coded to provide a visual queue with respect to its key properties; green is ideal, yellow-green is marginally cautionary, yellow is cautionary, and red represents a poor application. As noted, HfNbTaZr has a high yield stress of about 2,320 MPa at room temperature (RT) when properly annealed [Gorsse, Nguyen, Senkov, and Miracle, 2018; Feng, Surjadi, and Lu, 2020]. Its high yield stress is almost twice as large as Inconel 718 at RT, which is approximately 1,250 MPa. In addition, HfNbTaZr is expected to have good erosion and corrosion properties as a result of its Hf, Nb, Ta, and Zr content, with good strength at high temperature as a result of it four equiatomic refractory elements; refer to Table 2-1. Moreover, Nb and Ta provide HfNbTaZr a higher degree of creep resistance. Interestingly, Zr gives the RHEA excellent resistance to neutron and gamma irradiation damage, whereas Hf is a nuclear poison, with utility as a neutron absorber in the nuclear industry. Hf has a large number of protons (Z number), implying a strong ability to capture neutrons and gammas. Therefore, HfNbTaZr is suitable for non-reactor applications where high-temperature and/or high-

corrosion/erosion occurs, but where radiation is not an issue. Hence, suitable applications include components outside of the primary reactor system that are sufficiently away from the core, such as turbomachinery, heat exchangers, seals, bearings, and pipes, as well as any harsh-non-nuclear environments where radiation is not an issue.

Table 2-1. Some characteristics of the HfNbTaZr RHEA.

Refractory element / resistance to C=corrosion, Cr=creep, and R=radiation; S=high-temperature strength	Low thermal neutron absorption cross-section (<25 barns)	Low gamma absorption cross-section (based on Z, the atomic number)
Hafnium (Hf) / C, S	No / 104.0	<mark>72</mark>
Niobium (Nb) / C, Cr, R, S	Yes / 1.15	<mark>4</mark> 1
Tantalum (Ta) / C, Cr, S	Yes / 20.6	73
Zirconium (Zr) / C, R, S	Yes / 0.184	40

The HfNbTaZr alloy with no annealing or other post-process characterization was analyzed with a scanning electron microscope (SEM), energy dispersive x-ray spectroscopy (EDS), and electron backscatter diffraction (EBSD).

SEM is suitable for analyzing the surface of the material. Figure 2-1 shows a SEM image for HfNbTaZr with a ruler scale set to 50 microns. The image shows no significant spatial composition variations for the mixture (lower left-hand side (LHS) gray image) and the distributions for the elemental Ta, Nb, Zr, and Hf (the four central and right-hand side (RHS) colored images). Figure 2-2 shows a SEM image for HfNbTaZr with a ruler scale set to 5 microns.

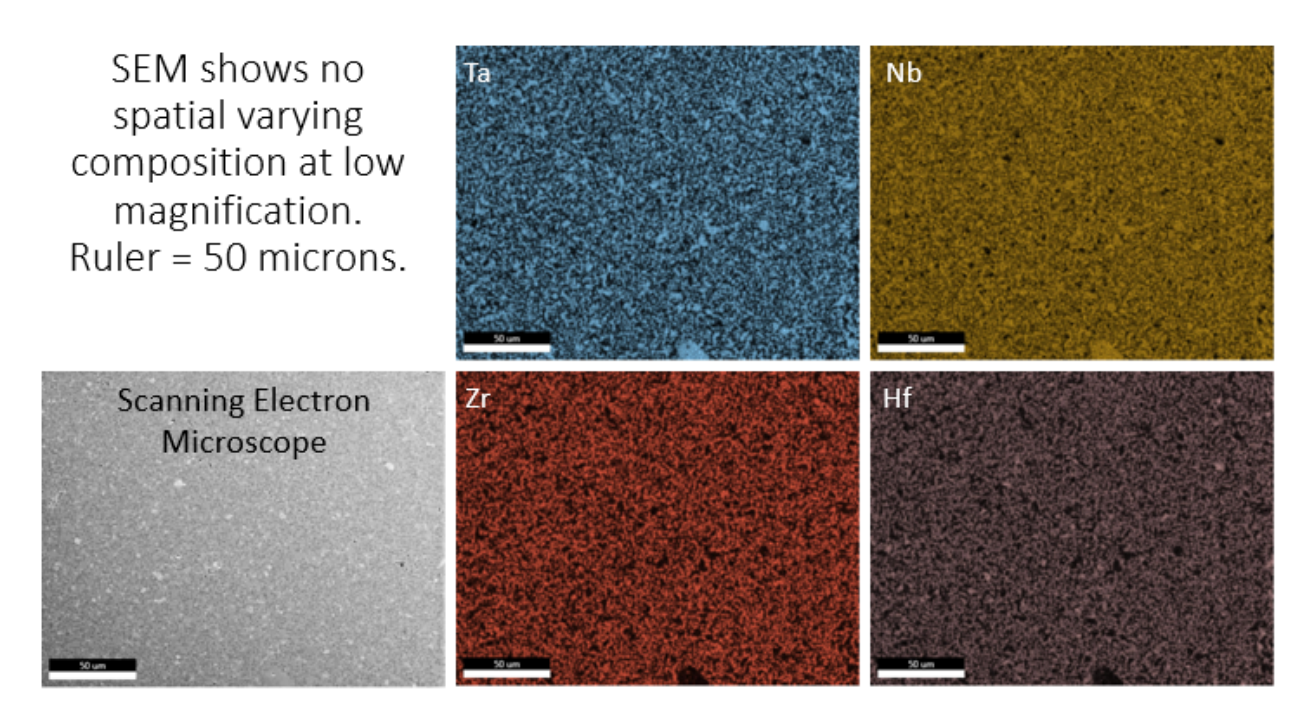


Figure 2-1. SEM image for HfNbTaZr with a ruler scale set to 50 microns.

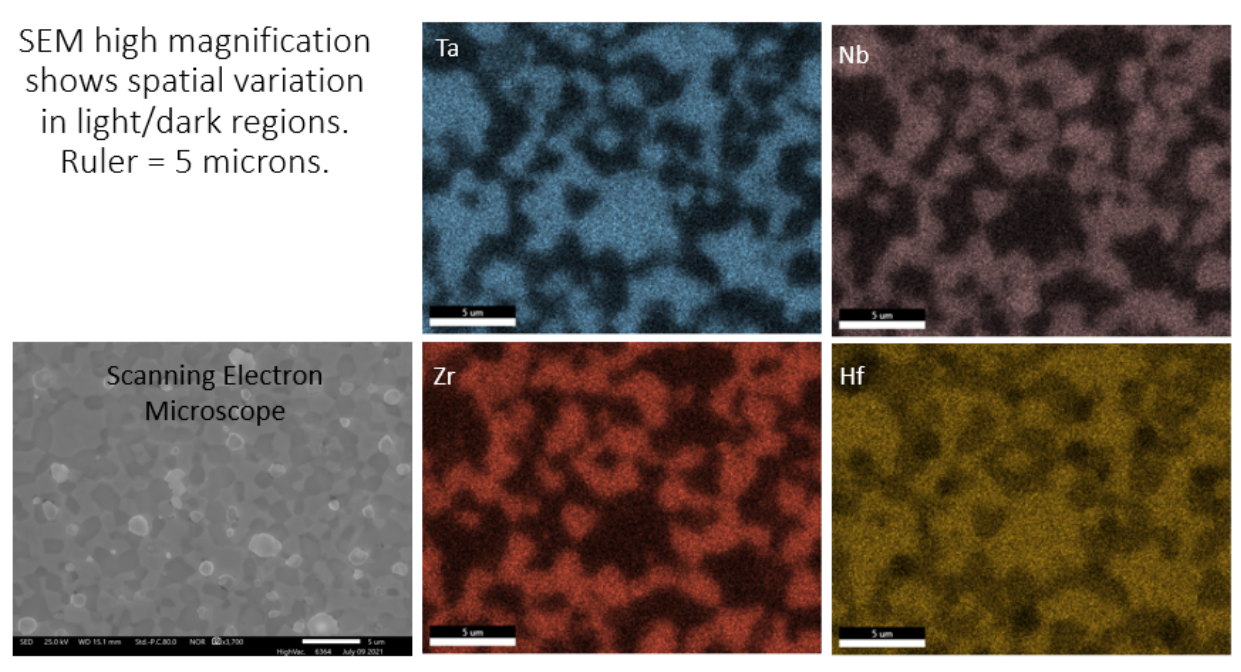


Figure 2-2. SEM image for HfNbTaZr with a ruler scale set to 5 microns.

EDS uses x-rays to analyze the elemental characteristics of the alloy in question. The EDS characterization confirmed the HfNbTaZr purity, as shown in Figure 2-3.

Finally, the test pieces were polished by grinding the specimens with different grit SiC paper to get rid of macroscopic scratches. Then, the samples underwent a chemical-mechanical polish with colloidal silica for 10 hours, until a highly reflective surface finish was achieved, as shown in Figure 2-4. This step is necessary to acquire EBSD images in the SEM and to obtain grain structure images.

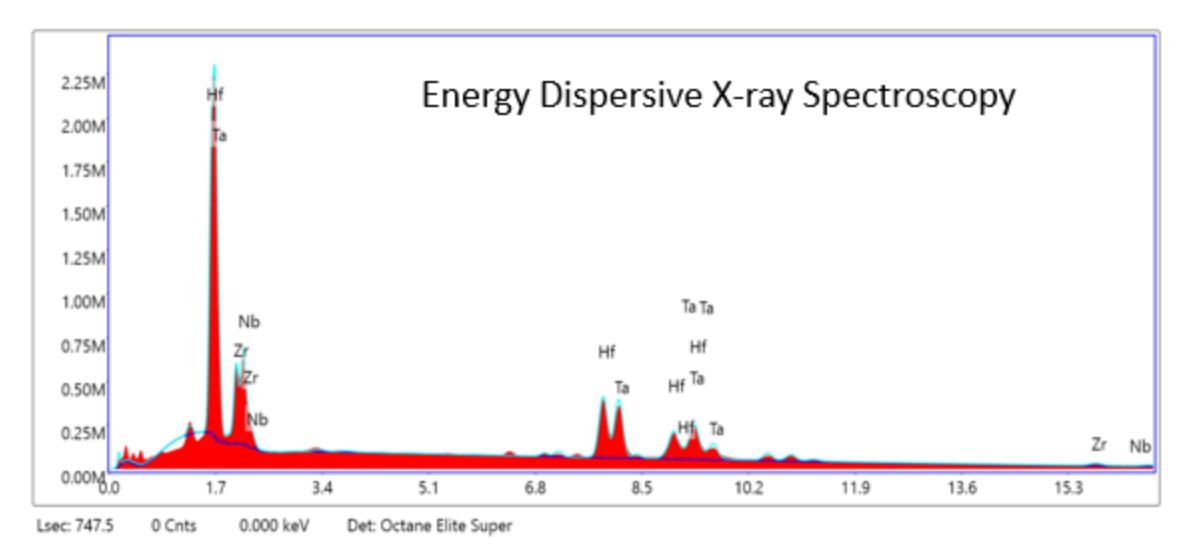


Figure 2-3. EDS image for HfNbTaZr.



Figure 2-4. Polished HfNbTaZr RHEA sample.

Figure 2-5 shows the EBSD images for the HfNbTaZr RHEA at 2 and 5 microns. EBSD is a SEM-based, powerful characterization technique that penetrates below the surface of the alloy to show crystal orientation, structure, grain boundaries, phase, lattice strain, etc. Figure 2-5 shows that the small-sized grain structures have a well distributed character. Moreover, the EBSD analysis determined that the HfNbTaZr RHEA had a body centered cubic (BCC) structure, which is a highly dense formation that is very desirable for material strength. Thus, the RHEA is well-mixed, with inhomogeneities only noticeable at the 2- to 5-micron scale, which correspond to the crystal length.

EBSD shows micron-sized grains indexed with BCC crystal structure

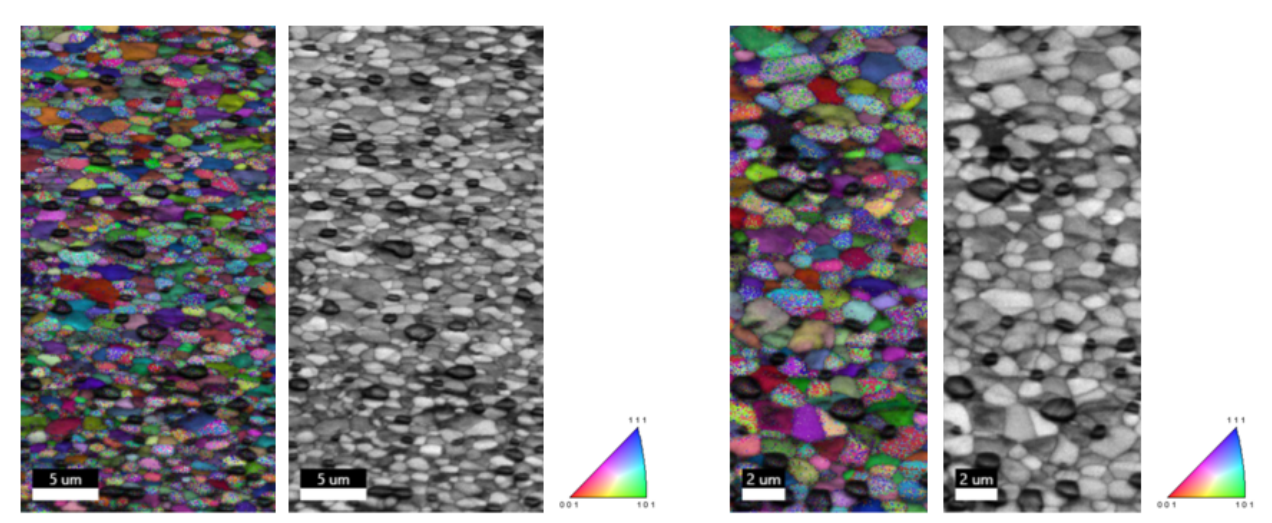


Figure 2-5. EBSD image for HfNbTaZr with a ruler scale set to 2 microns (RHS) and 5 microns (LHS).

2.2. The MoNbTaVW RHEA

For convenience, the material characteristics table for MoNbTaVW is also color coded, using the same guidelines described in Section 2.1. Table 2-2 shows that MoNbTaVW is relatively impervious to nuclear radiation, as compared with HfNbTaZr. In particular, Mo, Nb, Ta, V, and W have low thermal neutron absorption cross sections that range from 1.15 to 20.6 barns. In addition, except for Ta and W, which have a relatively high Z number of 73 and 74, respectively, the other three refractory-element Z ranges from 23 to 42. Therefore, it is expected that MoNbTaVW will be relatively resistant to radiation damage. Moreover, Mo, Nb, Ta, and W provide excellent corrosion resistance, while the five equiatomic refractory elements provide high strength at elevated temperature. Moreover, MoNbTaVW has shown excellent wear resistance compared with Inconel 718; recent experiments showed up 80% less wear [Poulia et al., 2017]. Finally, Mo, Nb, Ta, and W provide excellent creep resistance. Ironically, though W has the highest melting point of all the refractory elements, it increases brittleness at lower temperatures; thus, of necessity, a balance is made with respect to radiation and corrosion endurance, high-temperature strength, creep resistance, and degree of brittleness.

Table 2-2. Some characteristics of the MoNbTaVW RHEA.

Refractory element / resistance to C=Corrosion, Cr=Creep, and R=Radiation; S=high- temperature strength	Low thermal neutron absorption cross-section (<25 barns)	Low gamma absorption cross-section (based on Z, the atomic number)
Molybdenum (Mo) / C, Cr, R,	Yes / 2.6	<mark>42</mark>
Niobium (Nb) / C, Cr, R, S	Yes / 1.15	<mark>41</mark>
Tantalum (Ta) / C, Cr, S	Yes / 20.6	73
Vanadium (V) / R, S	Yes / 5.08	23
Tungsten (W) / C, Cr, S	Yes / 18.3	74

3. RHEA EXPERIMENTS AND DATA

For the RHEA IPL Project, it was endeavored to exceed the current size of manufactured RHEA components, to achieve a range of several inches, and to have the test pieces undergo rigorous experimental testing. This was achieved by leveraging Sandia's patents, technical advances, and previous experience working with RHEAs.

This section describes the RHEA test components that were subjected to radiation, erosion, thermal, and structural testing. The RHEA experimental performance data was compared with stainless SS 316 L, SS 1020, and Inconel 718 because they are currently present in many energy cycles and nuclear reactors, as well as many industrial applications.

3.1. Manufactured RHEA Test Coupons and Components

The following is a list of the HfNbTaZr and MoNbTaVW test pieces that were manufactured for this project during 2020:

- HfNbTaZr SPS disks (1 inch diameter x 1 mm thick); see Figure 3-1.
- HfNbTaZr SPS rectangular cuboid (1 inch x 1 inch x 1/16th inch); see Figure 3-2.
- HfNbTaZr SPS tube (1 inch length x 1 inch outer diameter x 0.109 inch thickness); see Figures 3-3, 3-13, and 3-14.
- MoNbTaVW LENS rectangular cuboid (1 cm x 1 cm x 1/16th inch); see Figures 3-4 and 3-5.
- MoNbTaVW LENS rectangular cuboid (1 inch x 1 inch x 1/16th inch); see Figure 3-6.
- HfNbTaZr spray coating over Inconel 718 and SS 321 substrates (8 to 9 mil) manufactured via the high velocity oxygen fuel (HVOF) method; see two LHS images in Figure 3-7 [Oksa et al., 2011].
- MoNbTaVW spray coating over Inconel 718 and SS 321 substrates (8 to 10 mil) manufactured via the HVOF method; see two RHS images in Figure 3-7.
- MoNbTaVW plasma spray coating over Inconel 718 and SS 321 substrates (10 to 12 mil) manufactured via the APS method; see two LHS images in Figure 3-8.
- HfNbTaZr plasma spray coating over Inconel 718 and SS 321 substrates (10 to 12 mil) manufactured via the air plasma spray (APS) method; see two RHS images in Figure 3-8.



Figure 3-1. HfNbTaZr SPS 1-inch disks.



Figure 3-2. HfNbTaZr SPS 1-inch rectangular cuboids.

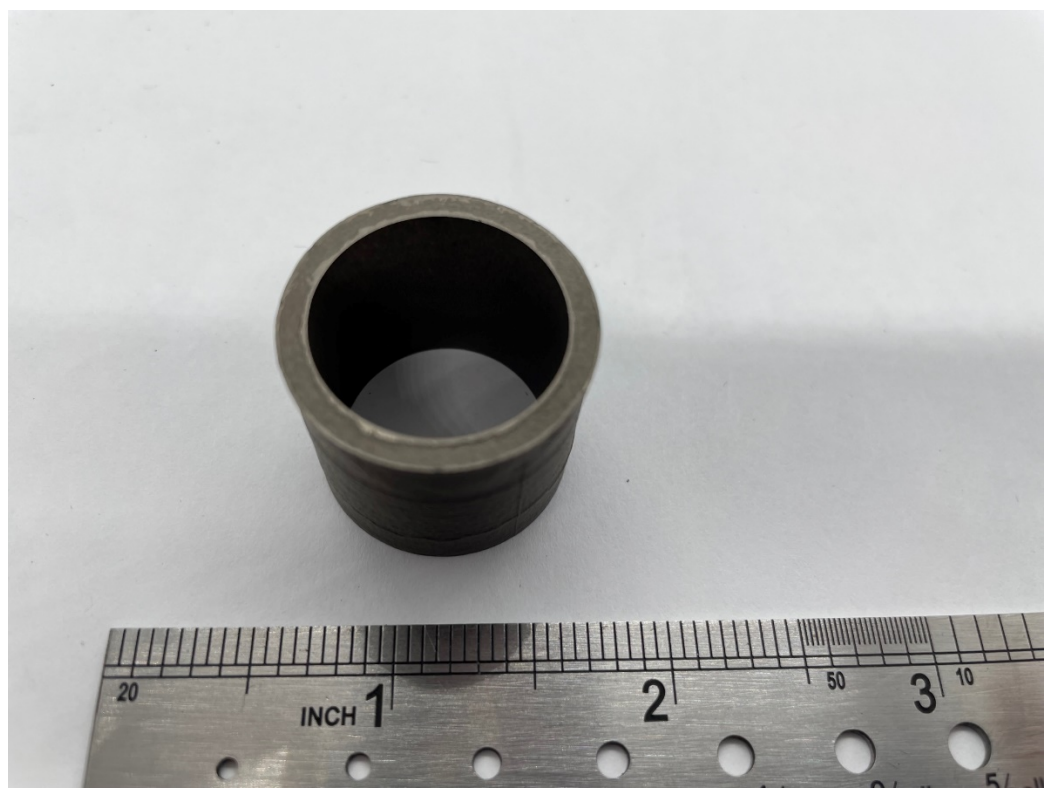


Figure 3-3. HfNbTaZr 1-inch SPS tube.



Figure 3-4. LENS MoNbTaVW rectangular cuboids (1 cm x 1 cm x 1/16th inch) as printed over a metallic substrate.

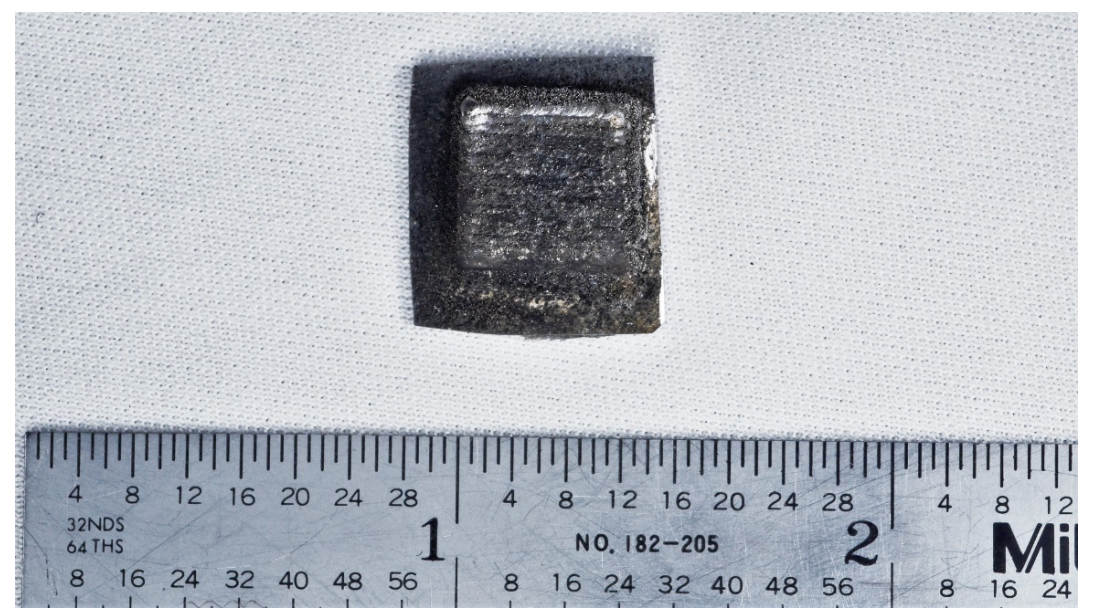


Figure 3-5. Detached LENS MoNbTaVW rectangular cuboid (1 cm x 1 cm x 1/16th inch) manufactured at 800 W.

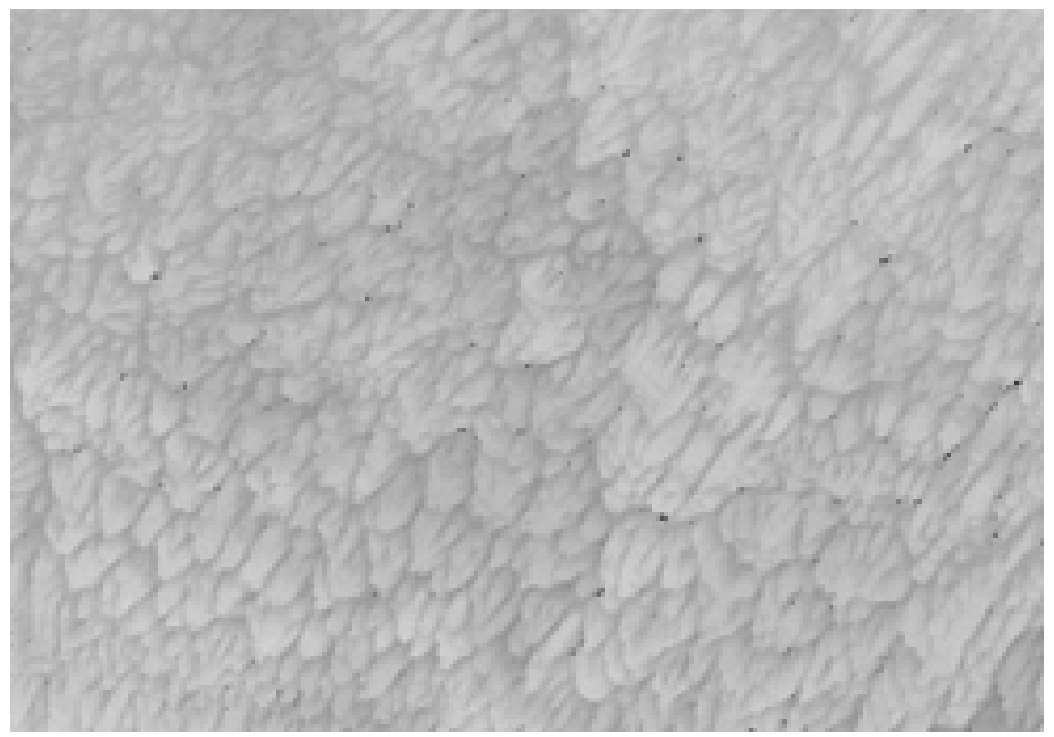


Figure 3-6. SEM image of LENS MoNbTaVW at 100 micron scale.

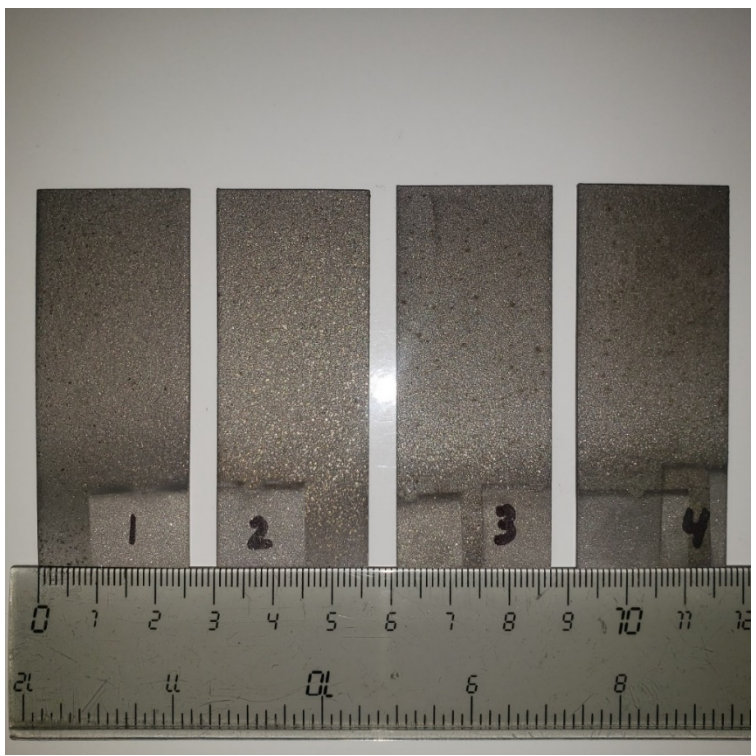


Figure 3-7. HVOF RHEA coatings. 1=Inconel 718 HfNbTaZr and 2=SS 321 HfNbTaZr; 3=Inconel 718 MoNbTaVW and 4=SS 321 MoNbTaVW.

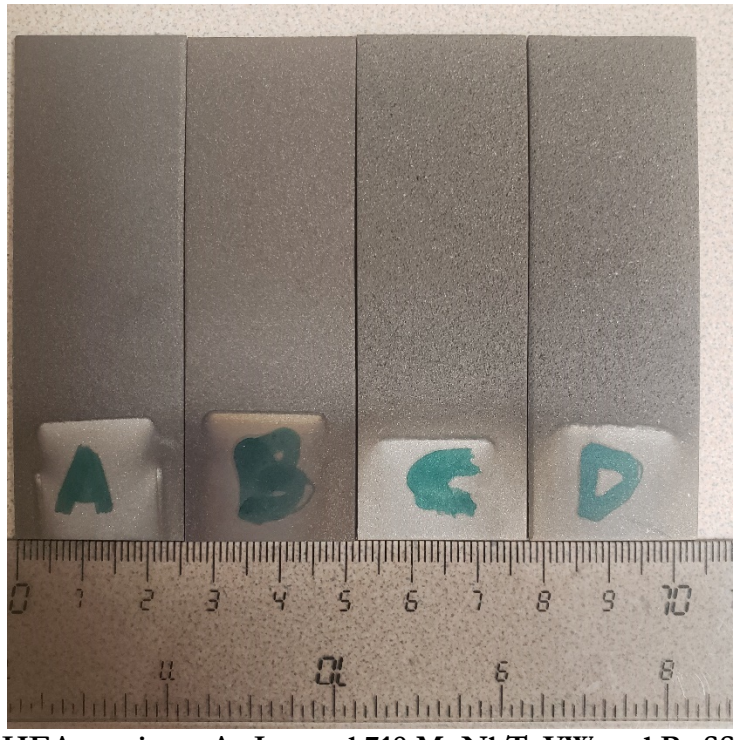


Figure 3-8. APS RHEA coatings. A=Inconel 718 MoNbTaVW and B=SS 321 MoNbTaVW; C=Inconel 718 HfNbTaZr and D=SS 321 HfNbTaZr.

The SNL LENS system is based on the laser beam directed energy deposition (LB-DED) method. The approach creates a part by feeding metallic powder through an extruder, then using a laser to melt the metal and deposit it on the surface of the part. This is a versatile and accurate process, which can be used to create new parts and repair broken parts (much like welding) [Locker, 2019]. LB-DED is fast and produces good material properties, though it generally produces a poor surface finish that requires postprocessing for critical dimensions. This method has extensive energy and facility requirements [Murray, 2020]. The method is conducted within an inert Ar atmosphere to minimize oxidation and contamination. Components created by LB-DED methods can suffer from high residual stresses formed during cooling, although these can be alleviated by adjusting the cooling rate or heat treatment.

For the LENS MoNbTaVW, 1 cm x 1 cm square pads were printed using LB-DED with premixed elemental powder targeting an equiatomic mixture. Laser power was controlled, ranging from 600 to 1000 W, with a constant scan velocity of 300 mm/min and a build strategy that involved a 90 degree crosshatch pattern between layers, with each layer having a serpentine pattern that was rotated by 90 degrees.

To complement the SNL LENS advanced manufacturing method, the SPS approach was used to synthesize HfNbTaZr through California Nanotechnologies [Eyerman, 2021]. The process started with pure Hf, Nb, Ta, and Zr powders in equiatomic ratios, which were then cryo-milled for eight hours in liquid nitrogen to form the HfNbTaZr powder. The material was then sintered at 45 MPa and 1,500 °C with a hold time of 10 minutes at maximum temperature and pressure. This process achieved a satisfactory manufactured density of 11.012 g/cm³ vs. 11.1 g/cm³, based on the theoretical value obtained by the rule of mixtures [Gorsse, Nguyen, Senkov, and Miracle, 2018]. Thus, the manufactured RHEA had negligible porosity. Upon manufacturing completion, a very thin, dark colored nano-sized carbon layer coated the surface of all the SPS samples. The SPS samples underwent a rigorous set of characterizations, to determine their composition and structure. The characterization shows a BCC microstructure with micron-sized grains, both of which indicate beneficial material properties (see Section 2.1). Chemical analysis shows no large inhomogeneities of the constituent elements and only micron-scale segregation. The achieved homogeneous microstructure and configuration are highly desirable for RHEAs.

For the sprayed coatings, no adhesion/diffusion barrier layers were required, as the coatings bonded well [Dixit, Rodriguez, Morgan, et al., 2021]. The HfNbTaZr powder was derived as an equiatomic mixture from the individual powders and mixed to form a relatively medium-mixed powder. A visual inspection of the coatings shows good adhesion and relatively fair homogeneity. Certainly, the coatings can benefit from well-mixed pre-alloyed powders.

Annealing has been found to increase the structural integrity of HEA coatings [Feng, Surjadi, and Lu, 2020], as well solid RHEA components [Miracle and Senkov, 2017]. Perhaps most importantly, the RHEA composition can become more homogenized after annealing, resulting in various benefits, including a higher potential for self-healing and higher resistance to harsh environments. For those reasons, most of the HfNbTaZr and MoNbTaVW test samples were annealed at Sandia using vertical heater elements, as shown in Figure 3-9. As noted by Miracle and Senkov, optimal annealing temperature and duration are still being investigated, and should be a focus of future research, given the potential benefits.

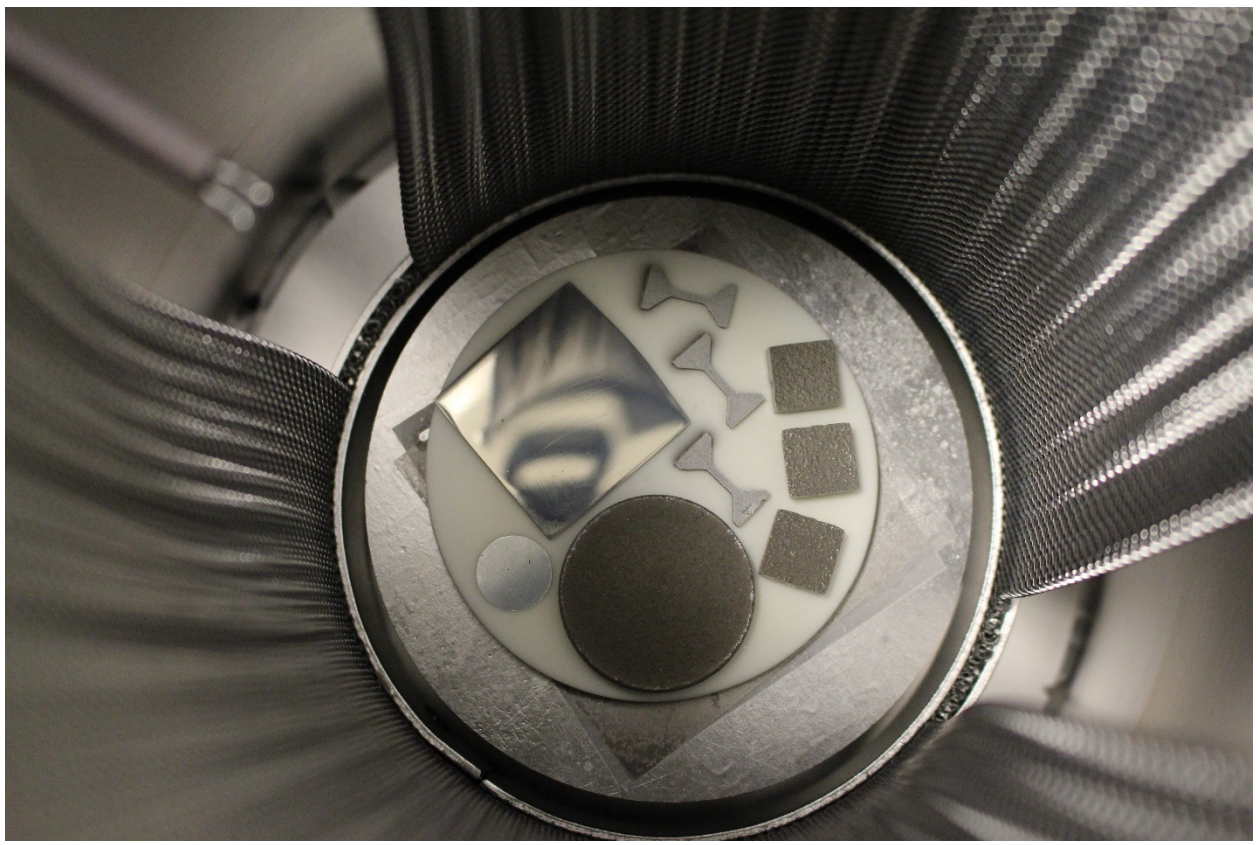


Figure 3-9. Annealed HfNbTaZr and MoNbTaVW test pieces.

3.2. RHEA Radiation Testing at the Ion Beam Lab

The SNL Ion Beam Laboratory (IBL) uses various types of ion species with energies at 10s of keV to 100 MeV, for accelerated radiation damage quantification of materials. The facility includes in-situ equipment for precise irradiation of the specimens, with the option of sequential and simultaneously undergoing high temperature laser-based heating and/or mechanical straining. In situ material characterization during this process can be achieved at both the meso and nano scales through SEM and transmission electron microscope (TEM) experiments, respectively. Figure 3-10 shows key IBL capabilities.

HfNbTaZr and MoNbTaVW test samples were irradiated with 2.8 MeV Au ions at the IBL. Additional samples were also irradiated with 14 MeV neutrons. For comparison purposes, SS 316 L and Inconel 718 were also irradiated with Au and neutrons, to serve as benchmark comparisons with the RHEAs. Because of the high levels of radiation from the irradiated samples, they are currently stored to allow sufficient decay time. Once that occurs, the materials will be examined, and the results will be reported.

Ion Beam Laboratory Capabilities

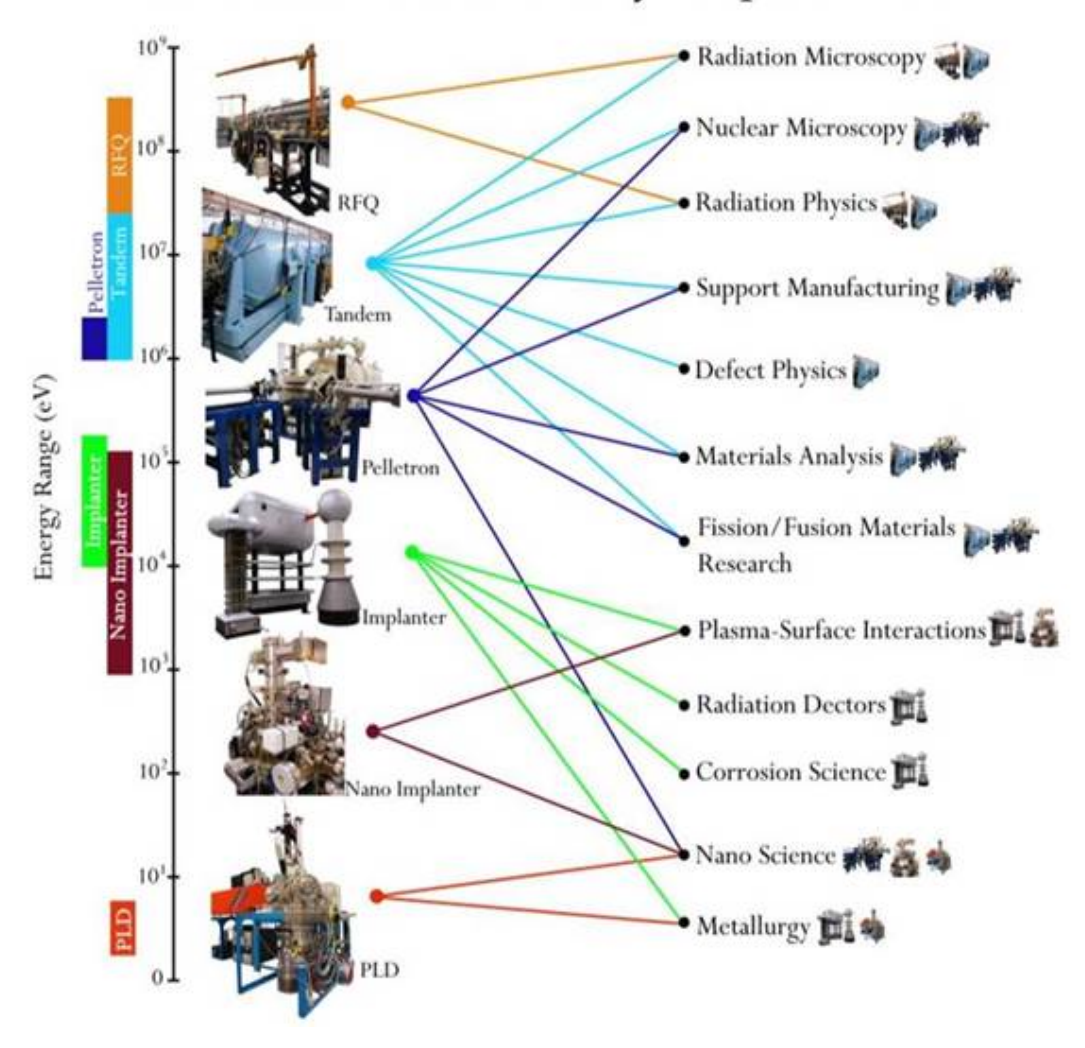


Figure 3-10. IBL capabilities.

3.3. RHEA Erosion Testing

As noted in Figure 5-1 of Section 5.2, sCO2 components can undergo significant erosion. Fortunately, RHEAs can have excellent erosion resistance, and these are investigated herein, and superb results are presented. ASTM G76 particle impingement experiments were performed to demonstrate the erosion resistance of the HfNbTaZr RHEA, as shown in Figure 3-11. A 1 inch by 1 inch HfNbTaZr surface at 175 °C was impinged by a particle jet driven at 85 m/s (190 miles per hour) using compressed N₂ gas. The N₂ was 99.995% pure, with less than 0.005% water. The particle flux rate was approximately 1.3 g/min-mm². The jet was perpendicular to the RHEA surface and lasted for 40 minutes. The particles consisted of 95 to 96% pure aluminum oxide with an angular shape with one or more sharp angles, and a mean size of 50 microns. The degree of erosion is then measured as weight loss per unit time.

The erosion tests were conducted on Inconel 718, SS 1020, SS 316, un-annealed (base case) HfNbTaZr, and annealed HfNbTaZr. All test pieces were 1 inch x 1 inch x 1/16th inch.

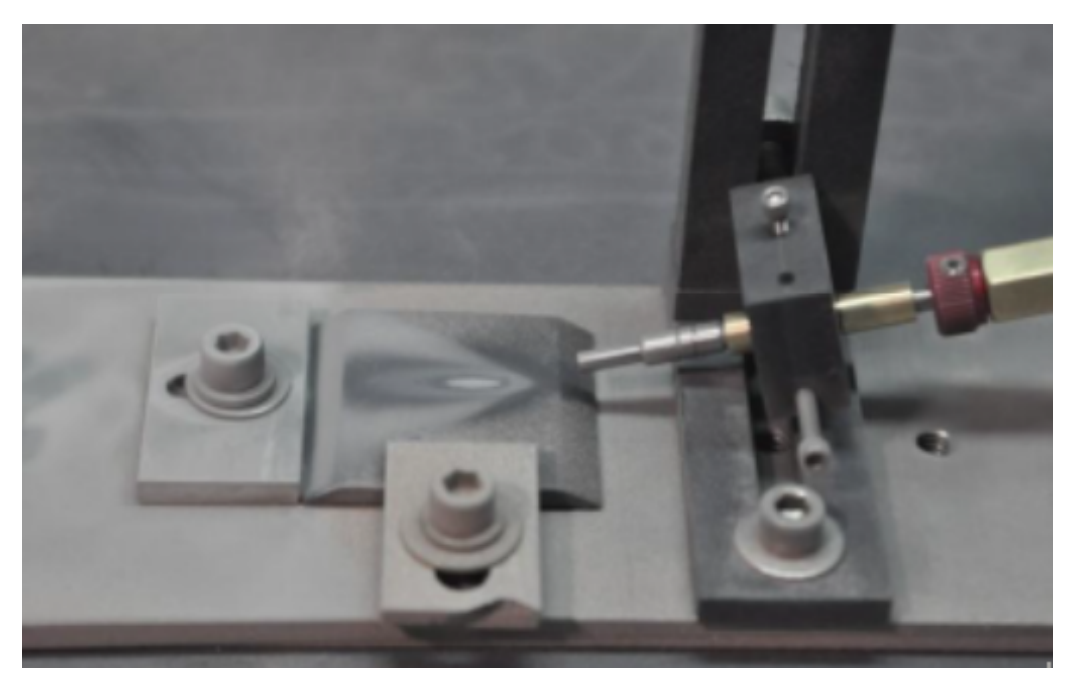


Figure 3-11. Erosion test set-up.

The erosion experiment results are shown in Figure 3-12. In particular, note that the best-performing HfNbTaZr RHEAs had 4, 8, and 14 times less erosion than SS 316, Inconel 718, and SS 1020, respectively. Moreover, the HfNbTaZr RHEA experienced no measurable erosion after 40 minutes under a particle jet blast at 190 miles per hour (85 m/s), vs. significant erosion for industrial grade Inconel and stainless steels. The postprocessing decreased the amount of erosion by a factor of 10 for the HfNbTaZr RHEA; more specifically, the eroded mass of the un-annealed RHEA was 10 times higher than that of the annealed RHEA. Therefore, the erosion data shows that we can solve the sCO2 Brayton Cycle erosion issue (e.g., diffuser vanes, turbine blades, bearings, seals, etc.). In Figure 3-12, RHEA 1 is the base-case HfNbTaZr composition with no postprocessing such as annealing or polishing, while various levels of postprocessing were applied to RHEAs 1A-1C.

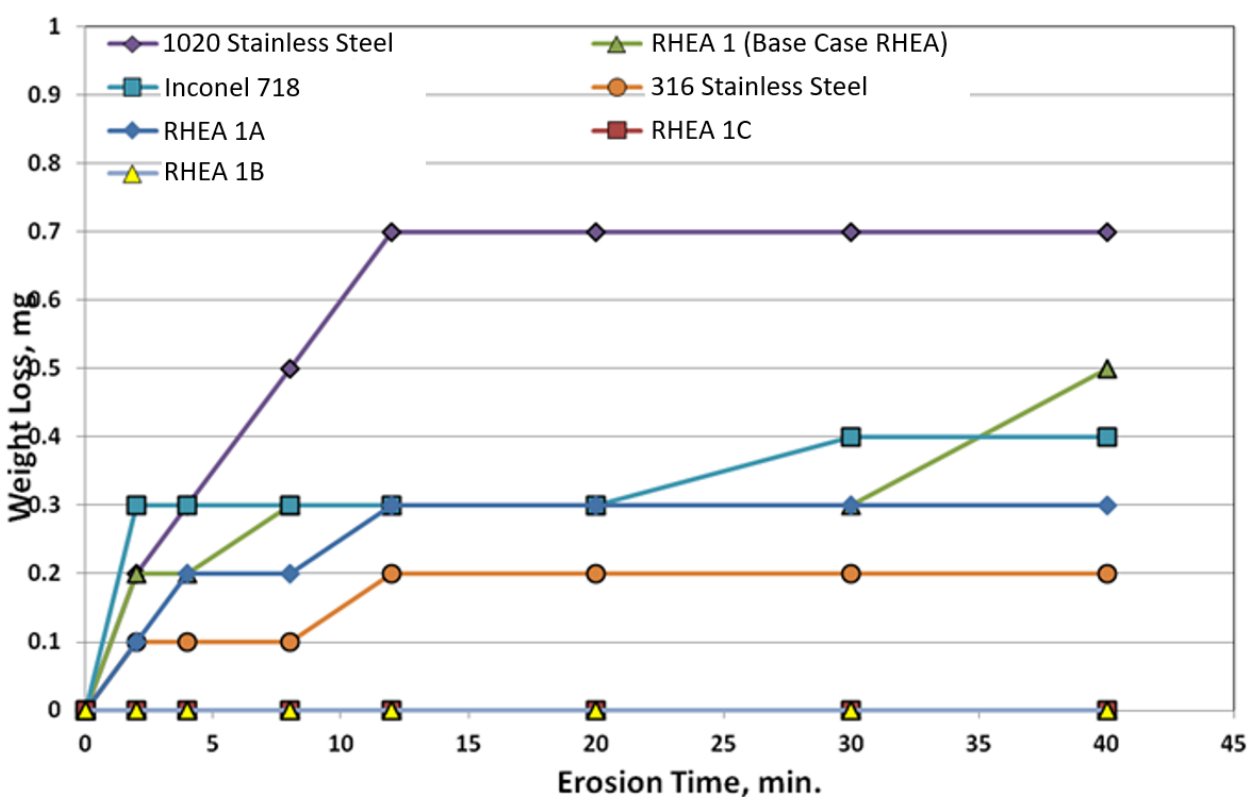


Figure 3-12. Cumulative eroded mass vs. time for the SS 1020, SS 314, Inconel 718, untreated base case HfNbTaZr, and three post-processed HfNbTaZr plates.

3.4. RHEA IBL Structural and Thermal Testing

In addition to radiation testing, Sandia's IBL testing is suitable for performing structural and thermal testing of small samples under compressive loads. The test piece is submitted to a given constant heat flux, which corresponds to a steady temperature.

3.5. RHEA Tube Manufacturing and Pressurization Test

Note that as far as the authors can tell based on the public literature, most, if not all RHEA test pieces manufactured anywhere in the world as of 2021 are in the few millimeter to centimeter range, if not smaller.

Because of its manufacturing simplicity, symmetry, and relevance to the energy industry, the chosen RHEA geometry is a cylindrical tube. Figure 3-13 shows the largest HfNbTaZr RHEA tube segment manufactured so far as of July 2021, and may well be the largest RHEA component manufactured so far anywhere in the world. The tube has a 1 inch outer diameter and length of 1 inch. Additional 1 inch tube pieces will be manufactured and bonded during August and September 2021, to culminate in a 4 inch tube that will be pressure tested and compared with Inconel 718. No structural issues are anticipated as a result of the bonding process. As noted previously, the manufactured density of the HfNbTaZr is 11.012 g/cm³ vs. the theoretical value of 11.1 g/cm³ [Gorsse, Nguyen, Senkov, and Miracle, 2018]. Annealing was performed to further increase the tube's structural strength and

homogeneity, and is shown in Figure 3-14. In addition, MoNbTaVW tubes will also be manufactured and tested.

For the pressurization experiment, one end of the RHEA will be capped and attached to the tube, while the other end will be connected to a pressurization test device via a Swagelok connector. As an alternative plan, a RHEA cylinder with an endcap can be manufactured, as a single piece. Another option is to manufacture the tube with NPT threading.



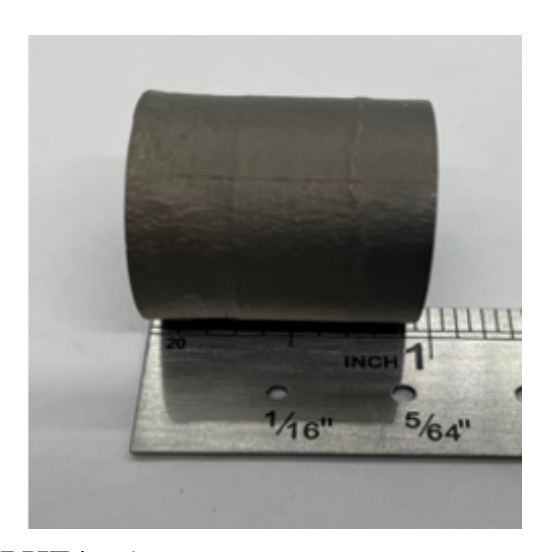


Figure 3-13. One inch HfNbTaZr RHEA tube segment.

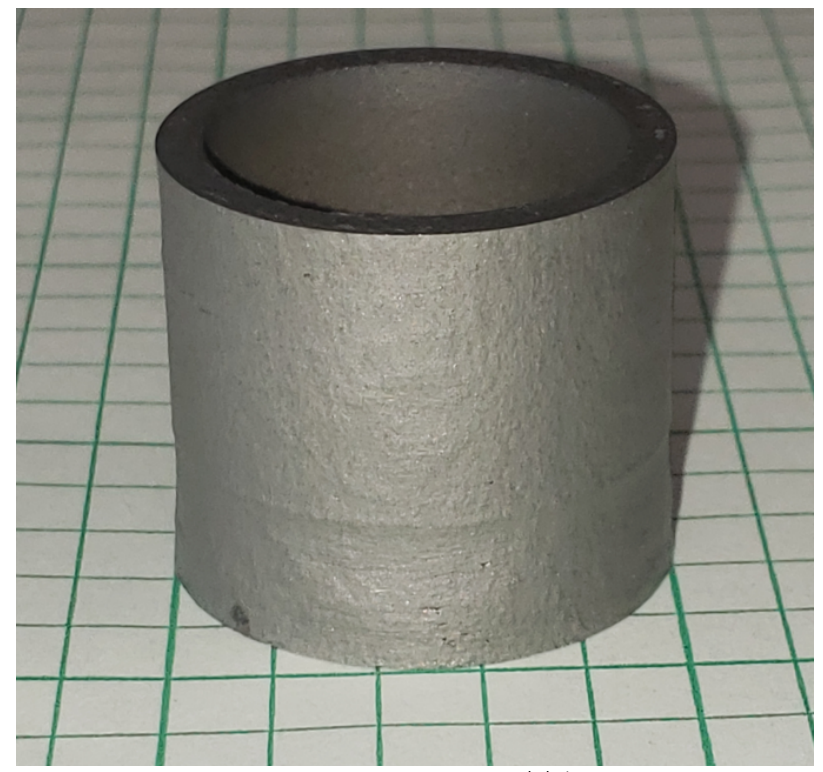


Figure 3-14. Annealed 1 inch HfNbTaZr RHEA tube.

3.6. RHEA Coating Experimental Data

Prior to testing, the specimens were epoxy-potted and polished to reduce surface roughness and to enable accurate measurements of scratch track dimensions. The methodology for the HfNbTaZr and MoNbTaVW RHEA thin coating characterization, which involved scratch tests and nanoindentation, is discussed next.

Scratch-based measurements of friction coefficient and low/single-cycle wear rate as a function of contact pressure were determined from linearly-ramped contact force experiments. These were measured as a function of deformation depth and probing regimes of elastic, plastic, and elastoplastic behavior, as shown in Figure 4. The dimensions of the tracks were determined by interferometric surface topographical mapping, and the combination of forces and wear track dimensions were used to determine friction behavior and wear resistance, as well as mechanical properties.

In one series of experiments, a spheroconical diamond tip (120 degree cone with 200 micrometer radius; Rockwell C type) was brought into contact and rastered against polished test coupons at a speed of 1 mm/s, while the applied contact force was ramped from 0 to 50 N, over a length of approximately 2.5 mm. The friction and surface-normal forces were independently measured, allowing for a calculation of the friction coefficient (ratio of friction and normal forces) and wear rate, which was determined based on the ratio of cross-sectional area of material displaced by the applied force; the results are shown in Figures 3-16 and 3-17.

RHEA coating ramped scratch $F_N = 0 - 50 \text{ N}$

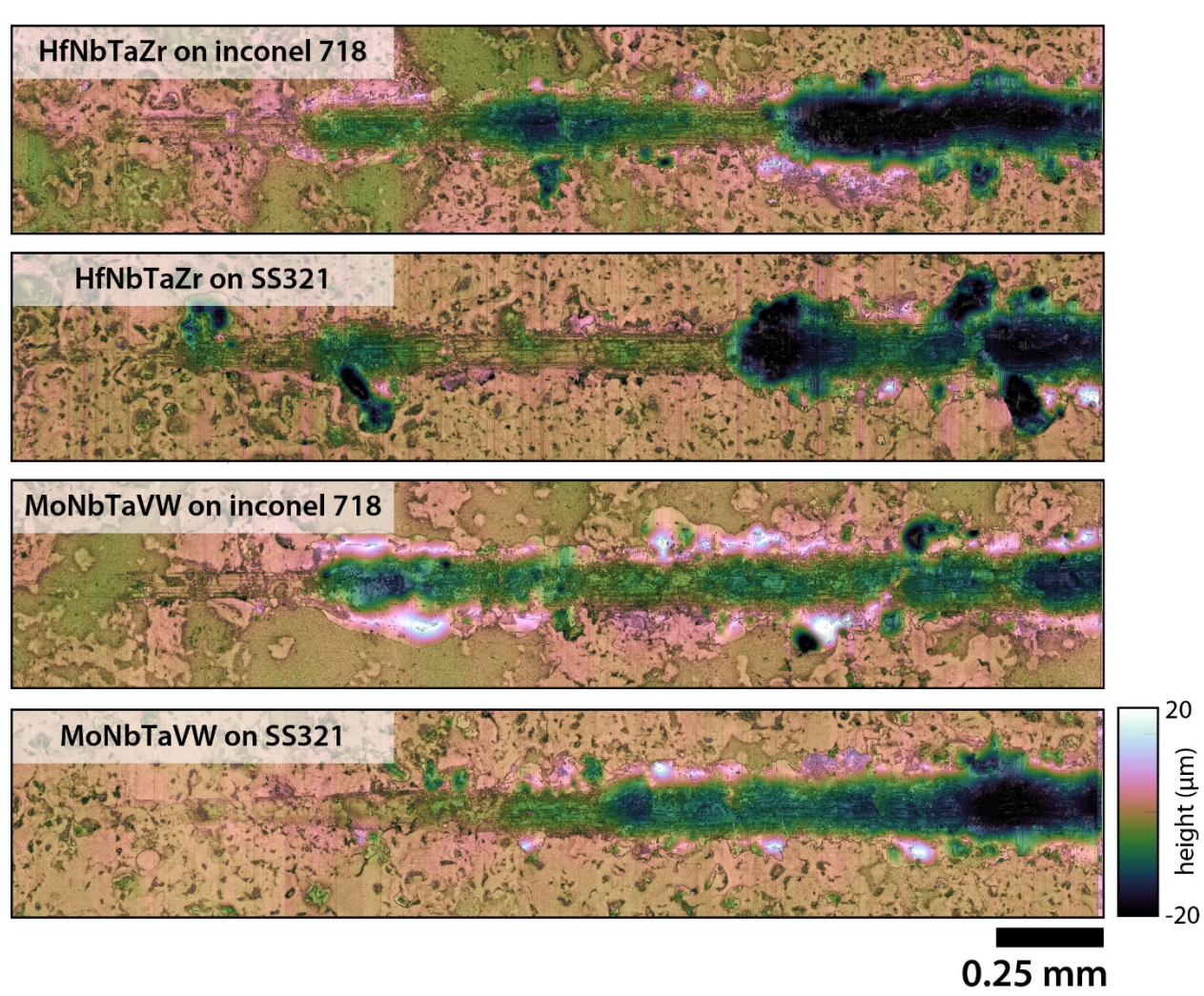


Figure 3-15. RHEA coating ramped scratch test.

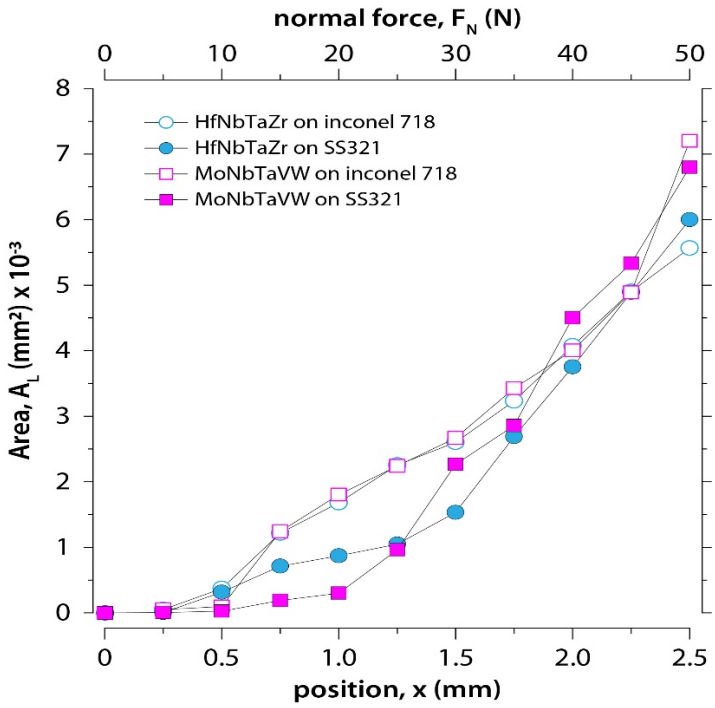


Figure 3-16. Applied normal force distribution in the four RHEA coatings.

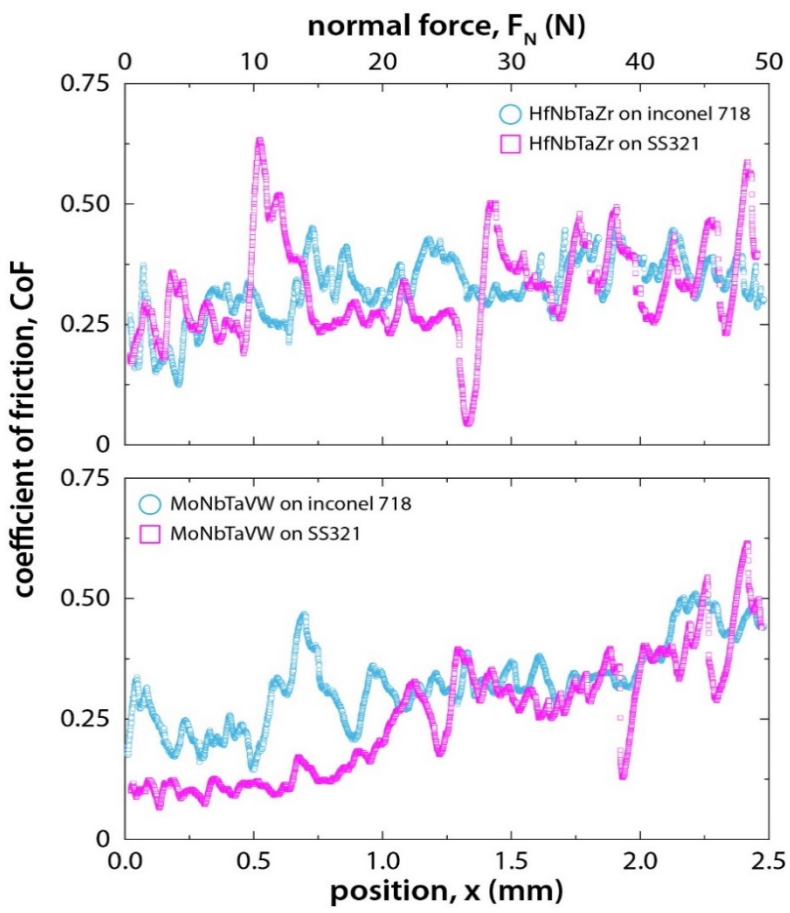


Figure 3-17. Coefficient of friction for the four RHEA coatings.

A series of constant force (50 N) scratches were performed at sliding speeds ranging from 0.001 mm/s to 10 mm/s. Using force data, tip geometry, and high-spatial resolution interferometric surface mapping, the strain rate-dependent hardness (H) and fracture toughness (Kc, in Mode II cracking) were determined by applying the methods described by earlier researchers [Hodge and Nieh, 2004; Nyakiti and Jankowski, 2010; Akono, Reis, and Ulm, 2011]. The strain rates were calculated following the convention of using the ratio of sliding speed to scratch track peak depth, hardness as the ratio of contact force to contact area, and fracture toughness as a function of projected frontal contact area and friction force. The micro/macro-scale measurements are complemented by nanoindentation measurements of hardness, using a stationary contact with ramped force and a Berkovich diamond tip (three sided pyramid geometry). Nanoindentation was used to determine depth-dependent hardness with higher spatial resolution, thereby probing variations in strength as a function of microstructural characteristics, such as phase type and grain size. The hardness for the four RHEA coatings is shown in Figure 3-18, which indicates a linear strain rate dependency over five decades.

For metals, the applied characterization methods have been shown to correlate well with traditional bulk techniques for determining yield or flow strength, including tensile testing, and Mode I fracture toughness in plane strain, such as accomplished by Charpy impact testing.

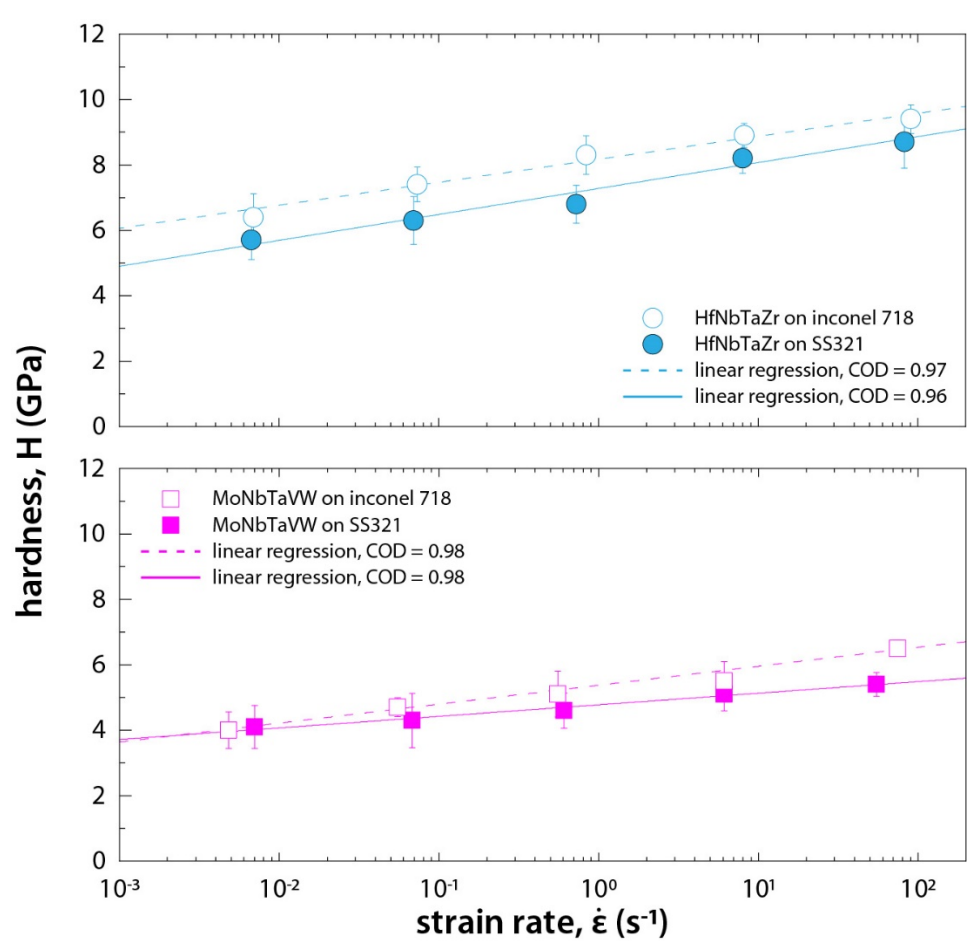


Figure 3-18. Hardness vs. strain rate for the four RHEA coatings.

A review of the literature indicates that the HfNbTaZr RHEA coating presented here is the first such manufactured based on the aforementioned, nearly-equiatomic elemental compositions, while the first MoNbTaVW coating was likely first manufactured in 2017 [Poulia et al., 2017].

The APS and HVOF processes were used to apply the RHEA coatings onto SS 321 and Inconel 718 because these alloys are prevalent in industrial applications. HfNbTaZr was selected because it is suitable for harsh environments that do not include nuclear radiation, while MoNbTaVW is suitable for harsh environments that include radiation.

Scratch and nanoindentation experiments were conducted to obtain experimental data to determine the friction coefficient as a function of applied force and position, as well as hardness as a function of strain rate. The experimental data shows excellent adhesive properties, high strength, reasonable homogeneity, and great deposition characteristics [Dixit, Rodriguez, Morgan, et al., 2021]. Most importantly, the experimental data indicates a strong potential for the application of these coatings to reduce erosion in sCO2 turbomachinery components, energy conversion, aerospace, and advanced nuclear reactors.

4. RHEA SIMULATIONS

For validation purposes and to gain more insights regarding RHEA applications, two key models were prepared. An Adagio code structural mechanics model was developed for the RHEA tube to compare with the pressurization test experiment. The model description and results are discussed in Section 4.1. In addition, a coupled CFD [Rodriguez, 2019] and structural model was developed to compare with the erosion experimental data [Fathi, 2021]. The results are discussed in Section 4.2.

4.1. RHEA Tube Pressurization Test Simulations

An implicit solid mechanics model was developed to compare the performance of RHEAs against commercial superalloys and to establish a starting point for computationally evaluating the performance of RHEAs for harsh environment applications. One- to four-inch long pressure vessels were chosen. The solid mechanics structural computational model applied a full eight-point integration scheme over the solid hexahedral elements, with a strongly objective strain incrementation and Cauchy stress measure [SIERRA, 2021].

A mesh was created, and the simulation applied a linearly increasing pressure value across the interior boundary. The value of the pressure ramped from zero to 1.0×10^9 Pa over the course of one millisecond. No boundary conditions were imposed on the exterior boundary. Apart from the pressure, the only other boundary condition was an inertia relief boundary condition, used to keep the model stabilized in space without fixing motion along any of the surfaces. This was applied over the entire mesh block. The HfNbTaZr RHEA tube structural model is shown in Figure 4-1.

Mesh Cutaway View

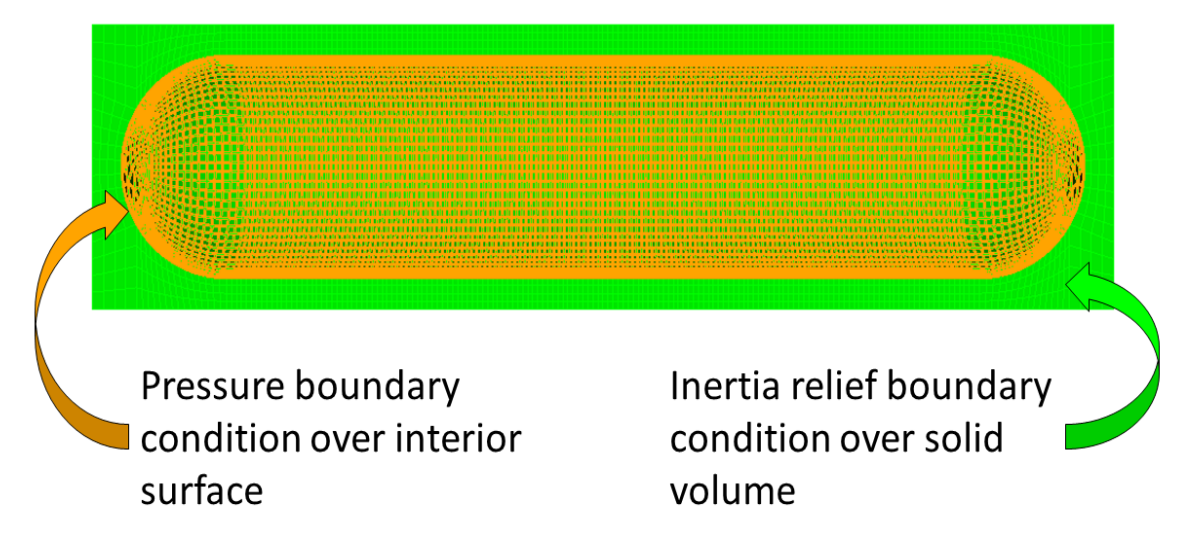


Figure 4-1. Adagio structural mechanics model for the RHEA tube.

Several material models were developed for Inconel 718, including a multilinear elastic-plastic failure model that uses a curve fit for tensile tests. Due to insufficient data for HfNbTaZr, only a linear elastic model was compared for the two alloys. Table 4-1 gives material properties used in the simulation for the two alloys.

Table 4-1. Elastic material properties of Inconel 718.

Parameter	Value	Notes
Density (g/cm³)	8.19 [Ametek, 2021]	Commercial product datasheet value.
Young's Modulus (GPa)	200.0 [Ametek, 2021]	Commercial product datasheet value.
Poisson's Ratio	0.294 [Maher, 2021]	Commercial product datasheet value.
Yield Stress (MPa)	655 [Ametek, 2021]	Commercial product datasheet value.

Table 4-2. Elastic material properties of HfNbTaZr.

Parameter	Value	Notes
Density (g/cm ³)	11.1 [Gorsse et al., 2018]	Estimated using rule of mixtures.
Young's Modulus (GPa)	100.0 [Qian et al., 2020]	Obtained from a nominal stress/strain curve for a tensile test of an annealed specimen.
Poisson's Ratio	0.38 [Gao et al., 2017]	Estimated using density functional theory.
Yield Stress (MPa)	860 [Qian et al., 2020]	Obtained from a nominal stress/strain curve for a tensile test of an annealed specimen, 0.2% offset.

HfNbTaZr appears to be a tougher alloy in the elastic region, with a lower Young's modulus and a higher yield stress, indicating that it is capable of enduring more stress and strain before permanent damage occurs. The properties of HfNbTaZr are less well-established in the literature than Inconel-718, though the values of the Young's modulus and yield stress are based on actual experimental data. However, it is also worth noting that Inconel 718 endures a much longer plastic strain region before failure than HfNbTaZr. In the most restrictive dataset from a series of tensile tests, the Inconel 718 specimen failed at a total engineering strain value of roughly 0.22 [Yanjin et al., 2015], while the HfNbTaZr specimen, even after annealing, failed at a total engineering strain value of roughly 0.02 [Qian et al., 2020].

Results from the linear elastic structural simulations agree with the above observations for the elastic strain region. Figures 4-2 and 4-3 show displacement and von Mises stress, respectively, for the Inconel 718 and the HfNbTaZr RHEA pressurization test tubes. These results were taken at the first timestep for which any element reached the material yield stress, after which the results of a linear elastic simulation become less physically applicable. As expected, the HfNbTaZr alloy is demonstrated to yield at a higher pressure and after greater elastic deformation than the Inconel 718 alloy. In particular, before reaching the material yield stress,

- HfNbTaZr underwent 2.5 times more displacement than Inconel 718
- HfNbTaZr tolerated 30% more pressure than Inconel 718

Note that these simulations are based on room temperature; for elevated temperatures, the HfNbTaZr structural integrity will continue to hold long after Inconel 718 has failed.

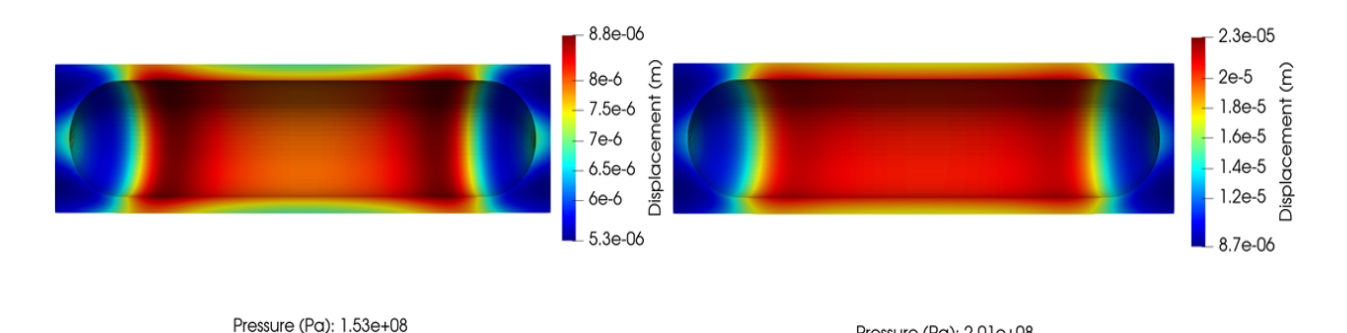


Figure 4-2. Comparison of displacement at yielding for Inconel 718 (left) and HfNbTaZr (right).

Pressure (Pa): 2.01e+08

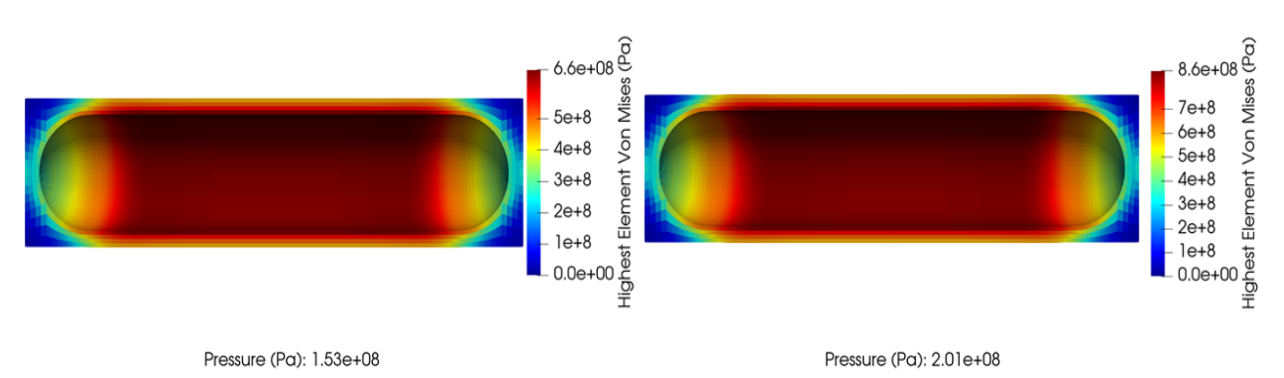


Figure 4-3. Comparison of von Mises stress state at yielding for Inconel 718 (left) and HfNbTaZr (right).

4.2. **RHEA Erosion Simulations**

Fluid-solid interaction (FSI) modeling and simulation of erosion using an Eulerian-Lagrangian particle-based approach was used to model a solid particle jet flow over HfNbTaZr, MoNbTaVW, SS 316 L, SS 1020, and Inconel 718 surfaces to simulate erosion. Based on the velocity and the shear stress provided from the CFD, the erosion caused by the solid particles was computed. The erosion procedure uses CFD/FSI using the ANSYS/Fluent code and the homemade code developed by the University of New Mexico (UNM) team to postprocess and evaluate the erosion [Fathi, 2021].

```
For the erosion simulations, the HfNbTaZr RHEA properties are as follows, E = 109 GPa, \rho = 11.1 g/cm<sup>3</sup>, and Vickers hardness = 365 HV.
```

For the MoNbTaVW RHEA, the material properties are as follows, E = 232 GPa, $\rho = 12.4$ g/cm³, and Vickers hardness = 536 HV.

The Multiphysics particle jet impingement model was validated first by simulating the erosion from an experiment where a water jet impinged on SS 316 [Pouraria et al., 2020]. The jet velocity was 14 m/s. The average particle diameter was 300×10^{-6} m. Figure 4-4 shows excellent agreement between the simulation output and the experimental data.

Then, the jet model was modified to simulate Inconel 718 and the HfNbTaZr RHEA. Figure 4-5 shows the N_2 gas fluid streamlines on the LHS, while the RHS shows the particle traces as they impinged and bounced off the Inconel and RHEA surface targets.

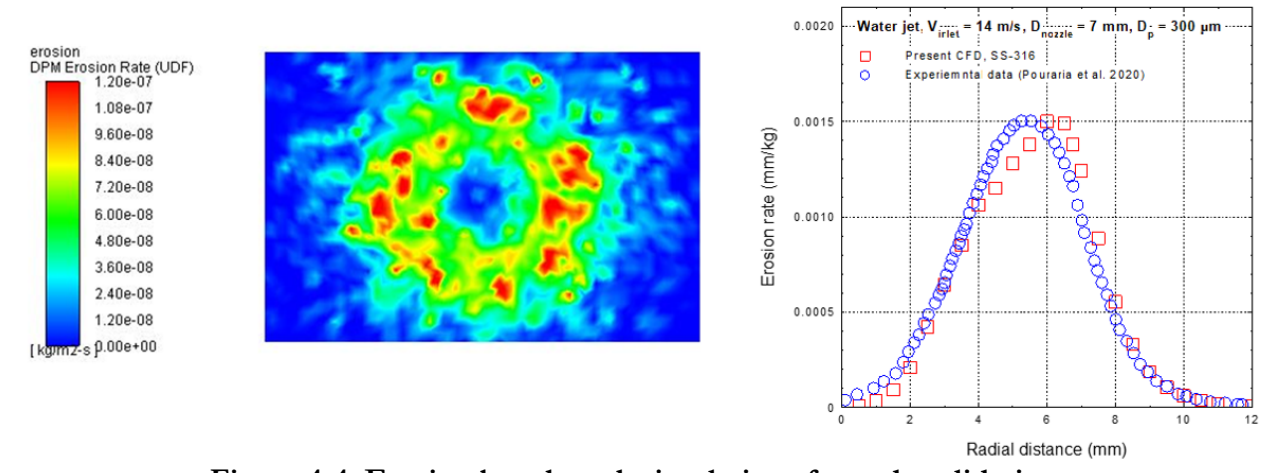


Figure 4-4. Erosion benchmark simulations for code validation.

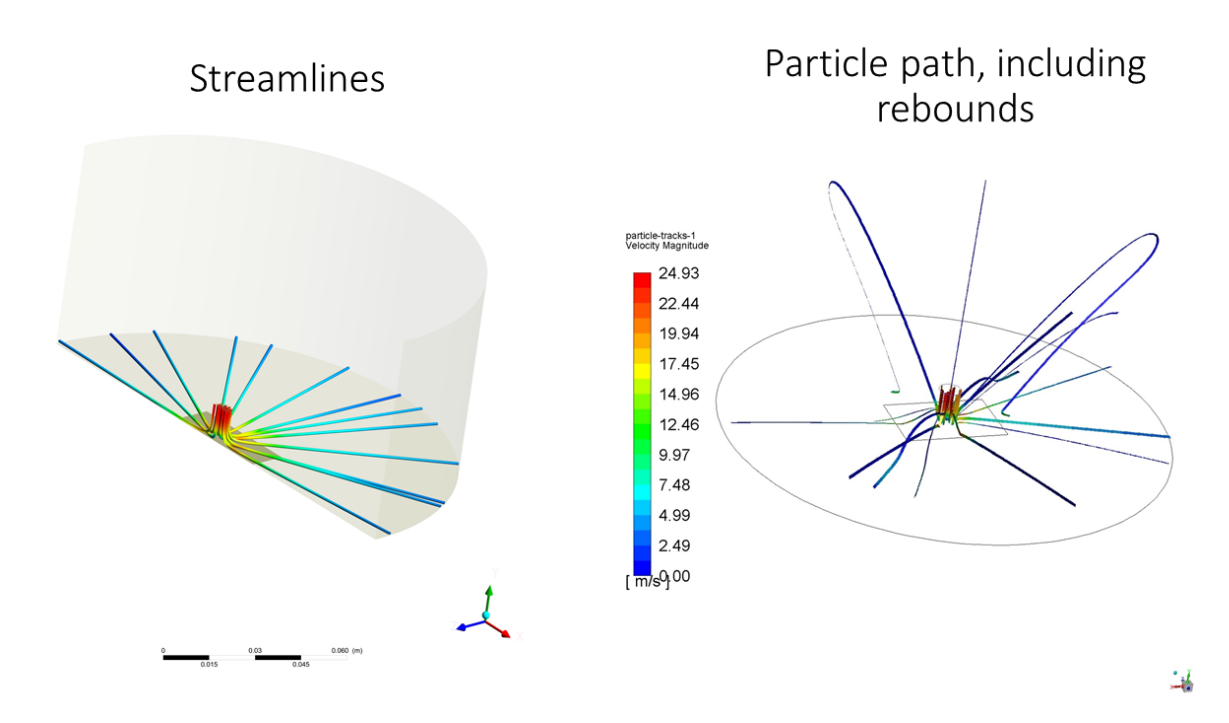


Figure 4-5. Erosion simulation model.

Finally, Table 4-3 shows the simulated erosion rate for HfNbTaZr, MoNbTaVW, and Inconel 718. Best-estimate and conservative modeling approaches were considered, so as to better characterize the models and to perform sensitivity studies with respect to the material properties and the experimental setup. As shown by the table, both the HfNbTaZr and MoNbTaVW RHEAs had a lower erosion rate than Inconel 718, with MoNbTaVW having the lowest erosion rate. More specifically, the conservative model shows that Inconel 718 had an erosion rate that was 1.24 and 1.55 times higher than HfNbTaZr and MoNbTaVW, respectively. In a similar fashion, the base case simulation showed that Inconel 718 had an erosion rate that was 1.20 and 1.53 times higher than HfNbTaZr and MoNbTaVW, respectively.

Table 4-3. CFD/FSI erosion simulation output.

	Erosion Rate (mg/min)		
	HfNbTaZr	MoNbTaVW	Inconel 718
Conservative Model	0.372	0.299	0.463
Base Case Model	0.261	0.205	0.314

5. RHEA APPLICATIONS

RHEA applications for near-term solutions involving advanced nuclear reactors, energy conversion cycles, and aerospace components have garnered much recent interest and bold solutions. This section discusses some near-term applications.

5.1. Advanced Nuclear Reactors

RHEA technology is expected to be a game-changer for the nuclear industry, not only because it will result in a significant performance increase, but because it will also provide solutions that can be used extensively in multiple industries. For example, high-temperature reactors challenge most state-of-the-art alloys and superalloys, because those materials have structural failure limits at temperatures of about 850 °C. Worst yet, some advanced reactors operate at high-temperatures and/or use corrosive fluoride/chloride salts or other highly corrosive fluids. Not only can certain RHEAs at the bench-scale survive temperatures at 1,200 to 1,600 °C, they also show outstanding corrosion-resistance properties. For instance, a bench-scale RHEA sample, HfNbTaTiZr, experienced essentially no corrosion after 240 hours exposure to boiling nitric acid [Jayaraj et al., 2017]. Similar corrosion-resistance is noted for bench-scale samples under sCO2 environments.

As an example of high-temperature applications, consider a commercial reactor, which typically operates at less than 700 °C (973 K). Its maximum theoretical thermal efficiency represents the maximum amount of useful energy that can be extracted. This is readily calculated using the Carnot thermal efficiency,

$$\eta_{Carnot} = \left(1 - \frac{T_{rej}}{T_{op}}\right) 100\%.$$

If the commercial reactor rejects its heat at 397 K, then the theoretical, maximum recoverable thermal efficiency is

$$\eta_{Carnot, Conventional} = \left(1 - \frac{397}{973}\right) 100\% = 59.2\%.$$

By contrast, the MS-VHTR operates at 1,200 °C (1,473 K). If its heat is also rejected at 397 K, its Carnot thermal efficiency is **13.8 percentage points higher** than the commercial, low-temperature reactor,

$$\eta_{Carnot, Advanced} = \left(1 - \frac{397}{1473}\right)100\% = 73\%.$$

Though the energy industry does not approach the Carnot efficiency, this serves as an example of the potential gains from high-temperature operation. For example, if a power plant makes \$1M profit per day, then just a 1% energy increase translates to \$3.7M additional income per year. That is, an efficiency gain of 13.8% yields an additional \$51.1M/year per plant. Because of their high structural integrity at very high temperatures, RHEAs can also enable accident tolerant fuels and cladding. This makes RHEAs ideal for high temperature reactors and reactors with highly corrosive coolants.

In summary, nuclear reactor RHEA applications include the following:

- Advanced high-temperature reactors (e.g., molten salt and gas)
- Micro reactors,
- Heat pipe reactors,
- Space reactors, and
- Accident tolerant fuels and cladding.

5.2. Energy Conversion Cycles

Recent advances at SNL offer the game-changing ability to apply the most promising RHEAs and to engineer their structural and thermal properties via controlled cooling rates, to significantly reduce, if not eliminate, turbine nozzle corrosion and pitting. However, should pitting occur, the self-healing properties of the RHEAs can significantly reduce micro cracks, whereby the strong interatomic forces in the high entropy materials reorient, thereby mitigating the defects. This extends the durability, efficiency, and reliability of turbomachinery components, as well as extends the lifetime of materials because of their enhanced ability to survive harsh environments.

Advanced sCO2 Brayton Cycles significantly increase nuclear, fossil, and solar power output, generally providing 43 to 55% thermal efficiency vs. about 38% for Rankine Cycles. However, sCO2 contains impurities that can pit and corrode the system, causing significant damage to the turbine nozzles and other components. This directly impacts the system's efficiency, safety, reliability, and maintenance requirements. For example, because of the harsh operational environment, gas turbines undergo heavy wear, necessitating regular maintenance.

It is common for power cycles to experience nozzle erosion and turbine degradation. Figure 0-1 (located in the Executive Summary) shows erosion in the airfoil vanes of an sCO2 turbine diffuser. The entire diffuser is shown on the LHS of the figure, while a 1/10th symmetry simulation of the vane is shown on the RHS. The solvent nature of sCO2 accumulates contamination particulates and transports them throughout the loop, thereby deteriorating surfaces as a result of high velocity impingement. These contaminants include metal particulates, small debris contaminants, oxides, and oils. Due to the fast rotation required of the turbine blades, the flow through the diffuser approaches Mach 1, thereby generating regions with high stress and impingement as the sCO2 flows through the diffuser vanes. Fluid-structure simulations using coupled CFD and structural analysis of the high-velocity flow and its associated contaminant particles show distortion and subsequent erosion in the thinner sections of the diffuser vanes, as shown in the RHS section of Figure 0-1. The central figure shows the significant levels of erosion that can occur in an sCO2 Brayton-Cycle diffuser [Fleming et al., 2014]. As noted in the central part of the region, impingement of high-velocity debris particles can cause significant erosion, resulting in costly shutdowns and repairs.

Consequently, the replacement of SS and Inconel components with RHEAs offers near-term solutions for Brayton Cycles that are much stronger than conventional nickel-based alloys and are therefore less abradable and more corrosion-resistant. Then, as the RHEA technology grows, most of the power conversion loop can be made from RHEAs. A clear example is a loop for space applications and RHEA heat pipes; Los Alamos National Laboratories has already tested various high temperature heat pipes that use refractory elements, including Mo, Re, and Ta [Reid et al., 2020].

6. SUMMARY AND CONCLUSION

An advantage of manufacturing sCO2 RHEA components is that RHEAs can have a material strength that exceeds SS 314 L and Inconel 718, all while operating at elevated temperatures that far exceed the capacity of the latter two. Another amazing capability of certain RHEAs is self-healing, whereby displacements per atom are reduced and micro damage (e.g., erosion) is reduced as the relatively strong interatomic forces reposition the material structure. These key RHEA traits can be huge in the energy industry because the service life of power conversion systems can be extended far beyond the current state-of-the-art, yielding power generation that is more reliable, requires less maintenance, and can operate at much higher thermal efficiency. For these reasons HfNbTaZr and MoNbTaVW RHEAs were manufactured and tested to compare key physical properties and performance with SS 316 L, SS 1020, and Inconel 718.

The material properties for the manufactured RHEAs, as well as the conducted erosion, structural, radiation, and high-temperature experiments demonstrated the superior performance of the RHEAs vs. SS and Inconel. In particular:

Manufactured RHEAs and their properties:

- HfNbTaZr was selected because it is suitable for harsh environments that do not include nuclear radiation, while MoNbTaVW is suitable for harsh environments that include radiation.
- HfNbTaZr and MoNbTaVW 1 cm x 1 cm and 1 inch x 1 inch cuboids were manufactured, as well as 1 inch dimeter disks. In addition, 1 inch HfNbTaZr tube solid segments were manufactured, and will be bonded to form a 4 inch tube during September 2021, and pressure-tested soon after.
- Thin RHEA coatings were applied onto SS and Inconel flat plate surfaces to test their adhesive capability and to increase erosion/structural performance.
- HfNbTaZr and MoNbTaVW coatings were successfully generated over SS 321 and Inconel 718 flat plate surfaces.
- A review of the literature indicates that the HfNbTaZr RHEA coating presented here is the first such manufactured based on the aforementioned, nearly-equiatomic elemental compositions, while the first MoNbTaVW coating was likely first manufactured in 2017.
- HfNbTaZr characterization analysis shows that the small-sized grain structures are well-distributed, with a BCC structure, which is a highly dense formation that is greatly desirable for higher material strength.
- The manufactured RHEAs are of excellent quality, as shown by inspection and characterization of their surfaces and interiors.
- Furthermore, the density of the manufactured HfNbTaZr is within 99.2% of the theoretical density.

Manufactured RHEA experimental data:

- The best-performing HfNbTaZr RHEAs had 4, 8, and 14 times less erosion than SS 316, Inconel 718, and SS 1020, respectively.
- The annealed HfNbTaZr RHEA experienced no measurable erosion after 40 minutes under a particle jet blast at 190 miles per hour (85 m/s), vs. significant erosion for industrial grade Inconel and stainless steels.

- The postprocessing decreased the amount of erosion by a factor of 10 for the HfNbTaZr RHEA; more specifically, the eroded mass of the un-annealed RHEA was 10 times higher than that of the annealed RHEA.
- The erosion data shows that we can solve the sCO2 Brayton Cycle erosion issue (e.g., diffuser vanes, turbine blades, bearings, seals, etc.).
- Scratch and nanoindentation experiments were conducted on the HfNbTaZr and MoNbTaVW RHEA coatings to obtain experimental data for the friction coefficient as a function of applied force and position, as well as hardness as a function of strain rate.
- The experimental data for RHEA coatings shows excellent adhesive properties, high strength, reasonable homogeneity, and great deposition characteristics, thereby indicating that RHEA coatings can be effectively used to protect Brayton Cycle components from erosion.

RHEA Multiphysics validation:

- The tube pressurization structural simulations show that the HfNbTaZr tube yields at a higher pressure, and after greater elastic deformation, than the Inconel 718 alloy.
- In particular, before reaching the material yield stress, HfNbTaZr underwent 2.5 times more displacement than Inconel 718; moreover, HfNbTaZr tolerated 30% more pressure than Inconel 718.
- A conservative CFD/FSI simulation shows that Inconel 718 had an erosion rate that was 1.24 and 1.55 times higher than HfNbTaZr and MoNbTaVW, respectively.

As a result of the experiments and simulations, the data shows the strong potential for RHEA HfNbTaZr and MoNbTaVW components and coatings as near-term solutions for wear, erosion, high-temperature strength, and radiation issues associated with sCO2 Brayton Cycles, turbomachinery, energy loops under harsh environments, and advanced nuclear reactors. Moreover, as a result of Sandia's manufacturing progress, these solutions can be implemented in the near-term, as cost-competitive and more robust solutions for energy, aerospace, and other industries that involve harsh environments.

The premise that certain RHEAs can significantly extend the durability, reliability, and thermal efficiency of the Brayton cycle and advanced reactors is further corroborated. Certainly, a reasonable level of additional modeling and experimentation is warranted, such as corrosion and creep studies; these are areas where recent literature advances indicate that various RHEAs also exceed the performance of current superalloys.

REFERENCES

- Akono, A-T., P. M. Reis, and F-J. Ulm, "Scratching as a Fracture Process: From Butter to Steel", Physical Review Letters, Vol. 106, DOI: 10.1103/PhysRevLett.106.204302, 2011.
- AT Kearney, "3D Printing: A Manufacturing Revolution", 2015.
- Baranova, A., "Russian Scientists Research Steel-Vanadium-Steel Laminate for Next-Gen Nuclear Reactors", ASM International, 2019.
- Corrosionpedia, "Refractory Metals: Properties, Types and Applications", https://www.corrosionpedia.com/2/1426/corrosion-101/refractory-metals-properties-types-and-applications. Accessed on June 4, 2021.
- Dixit, S., S. Rodriguez, M. R. Jones, P. Buzby, R. Dixit, N. Argibay, H. H. Lim, F. W. DelRio, and D. Fleming, "Refractory High-Entropy Alloy Thin Coatings for High Temperature Aerospace and Energy Applications", Journal of Thermal Spray Technology, 2021.
- Eyerman, E., "SPS HfNbTaZr Samples", California Nanotechnologies, Inc., email correspondence, 2021.
- Fathi, N., "CFD/FSI Erosion Analysis of RHEA, SS 316, and Inconel 718 Surfaces", University of New Mexico, 2021.
- Feng, X. B. et al., "Size Effects on the Mechanical Properties of Nanocrystalline NbMoTaW Refractory High-entropy Alloy Thin Films", International Journal of Plasticity, Vol. 95, pp 264-277, 2017.
- Feng, X., J. U. Surjadi, and Y. Lu, "Annealing-Induced Abnormal Hardening in Nanocrystalline NbMoTaW High-Entropy Alloy Thin Films", Materials Letters, Vol. 275, 2020.
- Fleming, D. et al., "Corrosion and Erosion Behavior in Supercritical CO2 Power Cycles", Proceedings of the ASME Turbo Expo 2014: Turbine Technical Conference and Exposition, GT2014, Germany, 2014.
- Gao, M. C. et al., "Computational modeling of high-entropy alloys: Structures, thermodynamics and elasticity", Journal of Materials Research, Vol. 32, 2017. https://www.osti.gov/pages/servlets/purl/1439970.
- Gorsse, S., M. H. Nguyen, O. N. Senkov, and D. B. Miracle, "Database on the Mechanical Properties of High-entropy Alloys and Complex Concentrated Alloys", Data in Brief, Vol 21, pp. 2664-2678, https://doi.org/10.1016/j.dib.2018.11.111, 2018.
- Hodge, A. M. and T. G. Nieh, "Evaluating Abrasive Wear of Amorphous Alloys using Nanoscratch Technique", Intermetallics Vol. 12, pp 741-748, doi:10.1016/j.intermet.2004.02.014, 2004.

- Jayaraj, J. et al., "Corrosion Behavior and Surface Film Characterization of TaNbHfZrTi High Entropy Alloy in Aggressive Nitric Acid Medium", Intermetallics, Vol. 89, No. 123, pp 123-132, 2017.
- Kim, H. et al., "Mechanical and Electrical Properties of NbMoTaW Refractory High-Entropy Alloy Thin Films", International Journal of Refractory Metals & Hard Materials", Vol. 80, pp 286-291, 2019.
- Liaw, P. K., "Radiation Behavior of High-Entropy Alloys for Advanced Reactors", University of Tennessee-Knoxville, 2014.
- Locker, A., "The Metal 3D Printer Buyer's Guide", All3DP, 2019.
- Maher, "Alloy 718 Data Sheet", Maher Limited 2021, accessed July 28, 2021. https://www.maher.com/media/pdfs/718-datasheet.pdf.
- Meghwal, A. et al., "Thermal Spray High-Entropy Alloy Coatings: A Review", J. Thermal Spray Technology, Vol. 29, pp 857-893, 2020.
- Metal, "Metal 3D Printing", 3D Hubs. Accessed on June 5, 2020. https://www.3dhubs.com/guides/metal-3d-printing/.
- Miracle, D. B. and O. N. Senkov, "A Critical Review of High-entropy Alloys and Related Concepts", *Acta Mater.*, Vol. 122, 2017.
- Mueller, F. et al., "On the Oxidation Mechanism of Refractory High-entropy Alloys", Corrosion Science, Vol. 159, 2019.
- Murray, J., "Low Cost Metal Additive Manufacturing", Desktop Metal presentation at Westwind Roadrunner3D in Albuquerque, NM, February 13, 2020.
- Murty, B. S., J. W. Yeh, S. Ranganathan, and P. P. Bhattacharjee, <u>High-Entropy Alloys</u>, Elsevier, 2nd Ed., 2019.
- Nagase, T. et al., "MeV Electron-Irradiation-Induced Structural Change in the BCC Phase of Zr-Hf-Nb Alloy with an Approximately Equiatomic Ratio", Intermetallics, Vol. 38, pp 70-79, http://dx.doi.org/10.1016/j.intermet.2013.02.009, 2013.
- Ngo, T. D. et al., "Additive Manufacturing (3D Printing): A Review of Materials, Methods, Applications and Challenges", *Composites Part B: Engineering*, Vol. 143, June 2018. https://www.sciencedirect.com/science/article/pii/S1359836817342944#fig3.
- Nyakiti, L. O. and A. F. Jankowski, "Characterization of Strain-Rate Sensitivity and Grain Boundary Structure in Nanocrystalline Gold-Copper Alloys", The Minerals, Metals & Materials Society and ASM International, Vol. 41A, pp 838-847, DOI: 10.1007/s11661-009-9996-9, 2010.Ametek, "Alloy 718 Datasheet", Ametek Specialty Products, accessed July 28, 2021. <a href="https://www.superiortube.com/-/media/ameteksuperiortube/files/products/materials/nickel-nicke

- alloys/stcalloy718.pdf?la=en&revision=537d1b39-f6f2-445f-85cd-c09953137b6c&hash=B997DEFFEC427E83B25FE13D0373F4C4&utm_source=&utm_mediu_m=undefined.
- Oksa, M. et al., "Optimization and Characterization of High Velocity Oxy-Fuel Sprayed Coatings: Techniques, Materials, and Applications", Coatings, Vol. 1, No. 1, pp 17-52, doi:10.3390/coatings1010017 2011.
- Poulia, A. et al., "Dry-Sliding Wear Response of MoTaWNbV High-entropy Alloy", Advanced Engineering Materials, Vol. 19, No. 2, DOI: 10.1002/adem.201600535, 2017.
- Pouraria, H. et al., "CFD Modelling of the Influence of Particle Loading on Erosion using Dense Discrete Particle Model, Wear., pp 460–461, https://doi.org/10.1016/j.wear.2020.203450, 2020.
- Printer, "Studio System Printer Specifications", Desktop Metal. Accessed on June 17, 2020. https://www.desktopmetal.com/uploads/DM-0003-Studio-System-Printer-Spec-Sheet-v4.2.1.pdf.
- Qian, H. et al., "Effect of Elemental Combination on Microstructure and Mechanical Properties of Quaternary Refractory Medium Entropy Alloys", Materials Transactions, Vol. 61, pp. 577 to 586, 2020. https://www.jim.or.jp/journal/e/pdf_open/61/04/577.pdf.
- Reid, R. S. et al., "Los Alamos Heat Pipe Lecture Series Notes", LA-UR-20-23592, Los Alamos National Laboratory, 2020.
- Rodriguez, S., "Current Capabilities at SNL for the Integration of Small Modular Reactors onto Smart Microgrids Using Sandia's Smart Microgrid Technology, High Performance Computing, and Advanced Manufacturing", Sandia National Laboratories, SAND2017-5537 R, 2017.
- Rodriguez, S., Applied Computational Fluid Dynamics and Turbulence Modeling: Practical Tools, Tips and Techniques, Springer International Publishing, 1st Ed., ISBN 978-3-030-28690-3, DOI: 10.1007/978-3-030-28691-0, www.cfdturbulence.com, 2019.
- Rodriguez, S., A. Kustas, and G. Monroe, "Metal Alloy and RHEA Additive Manufacturing for Nuclear Energy and Aerospace Applications", Sandia National Laboratories, SAND2020-7244, July 2020.
- Rodriguez, S., A. Kustas, and D. Ames, Non-Provisional Patent Application No. 17/062,136, "Highentropy Alloys, Refractory High-entropy Alloys, Methods of Selecting and Making, and Structures Formed from High-entropy and Refractory High-entropy Alloys", Sandia National Laboratories, 2020.
- Rodriguez, S., F. Gelbard, N. Argibay, A. Kustas, D. Adams, and D. Ames, "Refractory High Entropy Alloy Coatings for Safer and More Efficient Gas-Cooled Reactor Fuel", Sandia National Laboratories, 2021.
- Sciaky, "Benefits of Wire vs. Powder Metal 3D Printing", Sciaky Inc. Accessed on June 16, 2020. https://www.sciaky.com/additive-manufacturing/wire-vs-powder.

- Senkov, O. N. et al., "Refractory High-Entropy Alloys", Intermetallics, Vol. 18, pp. 1758-1765, 2010.
- Senkov, O. N. et al., "Development and Exploration of Refractory High-entropy Alloys—A Review", J. Mater. Res., Vol. 1, 2018.
- SIERRA Solid Mechanics Team, "Sierra/SolidMechanics 5.0 User's Guide", SAND2021-2961, Sandia National Laboratories, 2021.
- Wright, R., "New Alloy Material Approved for Use in High-Temperature Nuclear Plants", Idaho National Lab, 2020.
- Yanjin, L. et al., "Study on the microstructure, mechanical property and residual stress of SLM Inconel-718 alloy manufactured by differing island scanning strategy", Optics & Laser Technology, Vol. 75, pp. 197-206, December 2015. https://www.researchgate.net/publication/280643066 Study on the microstructure mechanic al property and residual stress of SLM Inconel-718 alloy manufactured by differing island scanning strategy.

DISTRIBUTION

Email—Internal

Name	Org.	Sandia Email Address
Kustas, Andrew	01832	akustas@sandia.gov
Lang, Eric	01881	ejlang@sandia.gov
Fleming, Darryn	08841	ddflemi@sandia.gov
Keith, Rodney	08841	rlkeith@sandia.gov
Mendez, Carmen	08841	cmmende@sandia.gov
Technical Library	01977	sanddocs@sandia.gov

Email—External

Name	Company Email Address	Company Name
Brian Robinson	brian.robinson@nuclear.energy.gov	Department of Energy

This page left blank



Sandia National Laboratories is a multimission laboratory managed and operated by National Technology & Engineering Solutions of Sandia LLC, a wholly owned subsidiary of Honeywell International Inc. for the U.S. Department of Energy's National Nuclear Security Administration under contract DE-NA0003525.